Solar Sailing Trajectory Design to Multiple Co-Orbital Near-Earth Asteroids

Cian Buckley

Technische Universiteit Delft

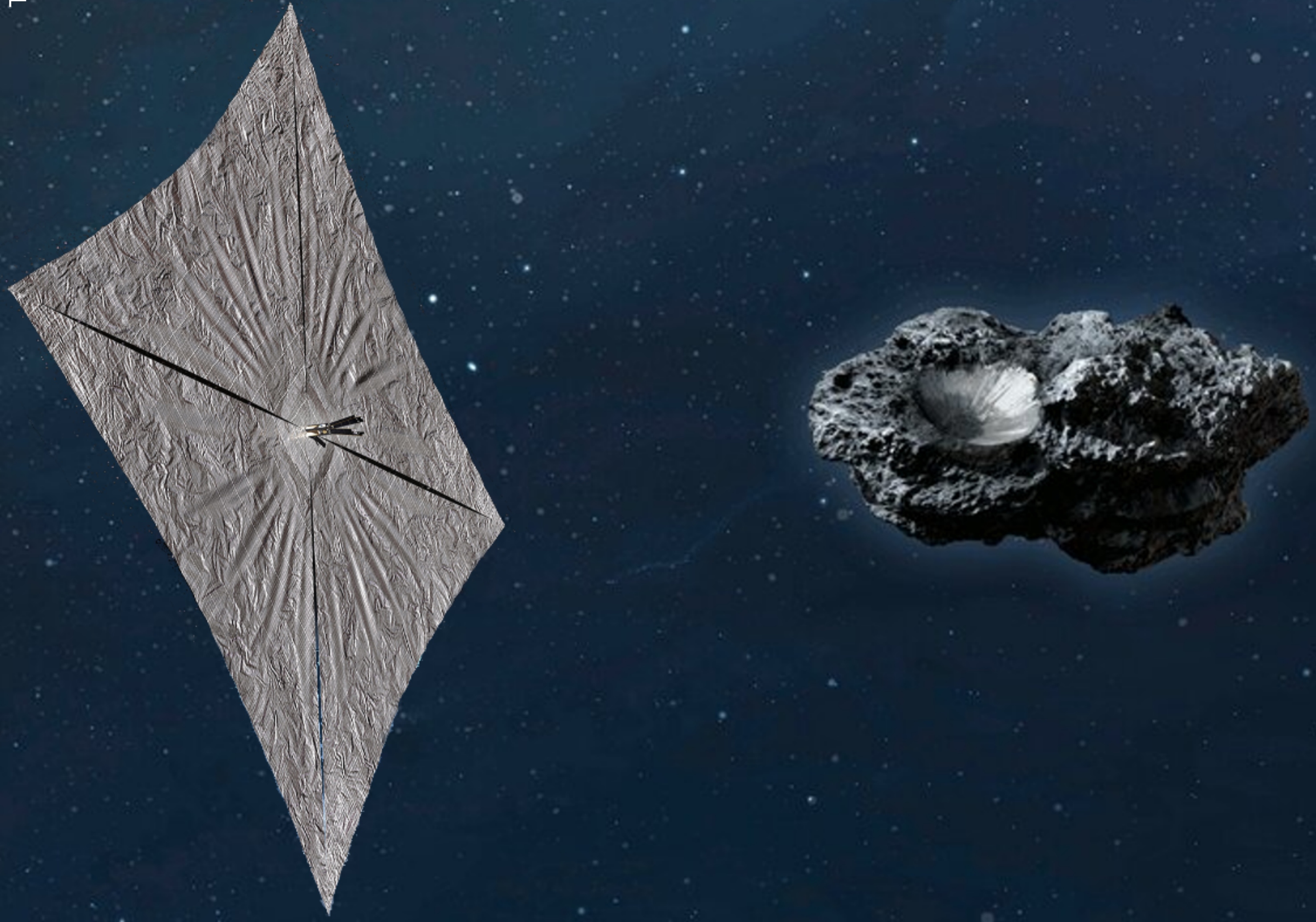

TU Delft

Solar Sailing Trajectory Design to Multiple Co-Orbital Near-Earth Asteroids

by

Cian Buckley

to obtain the degree of Master of Science
at the Delft University of Technology,
to be defended publicly on Wednesday September 28th, 2022 at 9:00AM.

Student number:	5368111	
Thesis committee:	Dr. D. M. Stam	Commitee chair
	Dr. M.J. Heiligers	Supervisor
	Dr. J Guo	External examiner

Cover image credits: ESA, Planetary Society
https://www.esa.int/ESA_Multimedia/Images/2020/06/Hera_and_its_asteroid_target,
https://www.planetary.org/articles/what-is-solar-sailing

Preface

This has been a long but (mostly) enjoyable journey throughout the two years of my Master's program. It has not been a typical two years, with a global pandemic doing its best to hinder anything at every chance it got. However, the adaptation from the university with online and remote learning has meant that there was little educational impact, and I am extremely thankful to the staff at TU Delft who have made online learning so accessible. Spaceflight has interested me for as long as I can remember, and once I discovered solar sailing through my courses, it was a clear choice for undertaking my thesis. This seemingly magic propulsion method has huge potential, and I am excited to see where the technology can go in future.

There are many people that I need to thank for helping me along the long road that has been my Master's degree. My girlfriend, Carrie, who has been supportive every step of the way, and has kept me on track those days where it seemed I would never finish. My family, who gave me the opportunity to study in Delft and follow my interest in Spaceflight. My thesis supervisor, Jeannette, who has been extremely helpful from the first day and has provided invaluable support and input along the way. The weekly meetings were essential to keeping me on track and progressing well. Finally, all of my friends who have supported me and listened to my complaints and rants over the last two years.

Cian Buckley
Dublin, September 2022

Executive Summary

Near-Earth asteroids are of particular interest for investigation from a range of fields of research. Many of these objects were created at the formation of the Solar System, and relative to the planets and larger bodies, they have undergone very little compositional change since then. Analysis of these asteroids can provide insight into the materials and processes present at the formation of the Solar System and the conditions that allowed life to form on Earth. Further, an impact from one of these asteroids could cause catastrophic damage on the Earth, so classification and analysis of the orbit of asteroids can allow for longer-term prediction of impacts and thus mitigation strategies. The limited resource availability on Earth could eventually drive the need to extract materials from extraterrestrial bodies. Knowledge of the composition of asteroids can allow for accurate selection of targets for space mining to provide these materials.

Co-orbital asteroids orbit the Sun in a near 1:1 mean motion resonance with the Earth, which means that the orbital distance of the asteroid, as well as the orbit time, is very similar to that of the Earth. Due to the similarity with the Earth's orbit, it has been suggested that these asteroids may possibly have formed at a similar time to the Earth. Analysis of these co-orbital asteroids may be able to allow researchers gain further insight into the mechanisms and processes surrounding the formation of Earth and the accompanying life. There have been a number of previous missions to near-Earth asteroids, both fly-by analysis missions and sample returns. However, to date there has been no mission specifically to a co-orbital asteroid.

Solar sailing is an increasingly popular low-thrust propulsion method for missions, due to the continuous and endless thrust generation capabilities. Solar sails use large, highly reflective surfaces known as sails to reflect incident solar radiation pressure and generate thrust. Maneuvering of the solar sail relative to the incident sunlight can control the direction in which the spacecraft travels. Solar sails require no fuel, and the total mission lifetime is limited only by the life of the sail itself. This propellant-less method of propulsion has been investigated for a wide range of applications, such as near-Earth asteroid rendezvous, interplanetary trajectories, or space debris removal.

The research undertaken in this thesis aims to build upon the previous research into solar sailing, especially theoretical missions designed to multiple near-Earth asteroids. The developed research objective of this thesis is *to find time- and encounter-optimal solar sailing trajectories to multiple co-orbital near-Earth asteroids*, and this objective is supported by three developed research questions. This research assumes an ideal sail model, which means that any effects due to absorption, diffuse reflection, thermal emission, or wrinkling are neglected, and the sail is assumed to specularly reflect all of the incident radiation. The dynamical model used for the motion of the solar sail assumes that only the Sun, and the Earth-Moon system exert gravitational influence on the spacecraft, and the only thrust acceleration comes from the solar sail.

A Monte-Carlo algorithm is developed which is capable of generating sequences of asteroids that can be visited using a fixed-angle control law for each transfer between asteroids. This means that the cone and clock angles which control the angle of the sail relative to the incident solar radiation are fixed for each transfer between target asteroids. This algorithm selects control angles of the sail at random through a Monte-Carlo search, and the solar sail trajectory with these angles is generated and analysed with regard to asteroid fly-bys. Tuning is performed on this algorithm, and it is ran a number of times to generate different sequences of asteroids to visit. These multiple runs are performed due to the random Monte-Carlo element of the algorithm, and the large variance in potential sail angles and target asteroids. Each of these multiple runs of the algorithm can result in a different sequence of asteroids to visit. Following the generation of a sequence, the first fly-by of this trajectory is optimised to reduce the relative fly-by distance and velocity, without compromising the subsequent fly-bys of the trajectory. This optimisation is performed with PSOPT, a pseudospectral collocation method implementation.

The developed sequence generation algorithm is capable of generating trajectories that encounter 18 asteroids within the nominal mission duration of 10 years, using near-term predicted technology levels for the solar sail. The optimisation of the first leg reduces the fly-by distance by 99.95% compared to the fixed control transfer, from $307,702$ km to 158.73 km, while the relative fly-by velocity was reduced

by 9.68%, from 4.79 km/s to 4.33 km/s. This high relative velocity is due to the set up of the sequence selection algorithm, which neglects relative velocity and considers only relative fly-by distance. Further analysis is performed on the first leg by removing the constraints on the fly-by time and optimising for the relative position and velocity. It is found that the velocity can be reduced to below 1 km/s, at the expense of a much further fly-by distance.

It can be concluded that the implementation of the sequence selection algorithm is capable of generating trajectories with many fly-bys, however the set up may result in sub-optimal fly-by velocities as the algorithm does not take the relative velocity into account. The optimisation method implemented through PSOPT can be considered suitable for this problem, as there is a significant reduction in fly-by distance and a slight decrease in fly-by velocity. Further work could be undertaken on the optimisation of the remaining fly-bys of the trajectory, or adapting the algorithm to include a relative velocity when considering fly-bys.

Contents

List of Figures

List of Tables

Nomenclature

List of Acronyms

ACS3	Advanced Composite Solar Sail System
AEP	Artificial Equilibrium Point
AIAA	American Institute of Aeronautics and Astronautics
AU	Astronomical Unit
CNEOS	Center for Near-Earth Object Studies
CR3BP	Circular Restricted Three Body Problem
CR3BPS	Circular Restricted Three Body Problem with Solar Sailing
ER3BP	Elliptical Restricted Three Body Problem
IKAROS	Interplanetary Kite-craft Accelerated by Radiation Of the Sun
IMAP	Interstellar Mapping and Acceleration Probe
JAXA	Japan Aerospace Exploration Agency
JPL	Jet Propulsion Laboratory
NASA	National Aeronautics and Space Administration
NEA	Near-Earth Asteroid
NEO	Near-Earth Object
RNG	Random Number Generator

List of Symbols

Latin Symbols	
$\mathbf{a}$	Acceleration vector
m	Small body
m_1, m_2	Primary bodies
m_E	Mass of Earth
m_M	Mass of Moon
m_S	Mass of Sun
$\mathbf{r}$	Position vector within $C(x, y, z)$
U	Effective potential
$\mathbf{x}$	State vector
Greek Symbols	
β	Lightness number
λ_a	Mean longitude of an asteroid
λ_p	Mean longitude of a planet
μ	Mass ratio
Ω	Right ascension of the ascending node
ω	Argument of periapsis
ϕ	Mean longitude difference
$\pm\tilde{\lambda}$, $\pm i\tilde{\omega}_i$	Eigenvalues
$\boldsymbol{\omega}$	Angular rotation vector
θ	True anomaly
U	Effective potential

1

Introduction

This chapter introduces the work undertaken in the thesis. Firstly, the relevance of the thesis work is described in section 1.1, where the targets, co-orbital near-Earth asteroids, are described. Following this, the concept of solar sailing is described, along with some background surrounding the development of solar sailing, in section 1.2. The research objective and related questions of this thesis work are defined in section 1.3. Finally, the structure of the entire thesis report is provided in section 1.4.

1.1. Co-Orbital Near-Earth Asteroids

A near-Earth Object (NEO) is generally defined as any asteroid or comet whose orbital approach brings it to within 1.3 Astronomical Units (AU) of the Sun [1]. Both asteroids and comets are remnants from the formation of the solar system, but asteroids consist of metals and rocky materials and are located nearer the Sun, while comets consist of ice, dust, rocky materials and organic compounds and generally originate in the outer solar system [2]. According to the National Aeronautics and Space Administration (NASA) Jet Propulsion Laboratory (JPL) Center for Near-Earth Object Studies (CNEOS), over $29,000$ near-Earth asteroids (NEAs) that have been detected as of August 2022[1].

1.1.1. Reasons to Visit Asteroids

It is known that the solar system formed from a disk of gas, dust, and particulate matter orbiting our Sun. Past studies of meteorite samples have shown that this was a relatively fast process, occurring over a timescale of at most a few million years [3]. However, the composition of these materials in the early solar system is not exactly known, due to the compositional changes that the planets underwent during development, due to the high temperatures and pressures present [4]. Similarly, the processes that allowed for the formation of life on Earth are unclear. It is unknown whether life developed from the materials that were present during the formation of Earth, or if the source was an extraterrestrial delivery mechanism in the form of an asteroid, comet or similar. Multiple scenarios and possibilities have been theorised and shown to be feasible, but there is no clear evidence for one specific mechanism [5].

Asteroids that were created during the formation of the solar system may be able to provide insight into the primitive materials present during this period. Further knowledge and analysis of these asteroids may therefore be able to deepen our understanding of the processes surrounding the formation of the Earth and other planets, and the conditions with which life on Earth could form. It is therefore desirable to analyse asteroids to gain more information on their compositions and similar properties, the easiest of which to visit will be the NEAs as they are closest to Earth.

Another reason for visiting and analysing NEAs is for the purpose of planetary defence. If a large enough asteroid were to impact the Earth the effects could be catastrophic for human population, either local or global depending on the impact, and even asteroids less than 20 meters in diameter can cause fatalities [6]. Visiting a NEA allows for closer analysis and thus more certainty in the composition and properties. This allows for more accurate classification of the asteroid and its orbital parameters.

---

[1] Jet Propulsion Laboratory. CNEOS Discovery Statistics. Available at `https://cneos.jpl.nasa.gov/stats/totals.html`. [Access Date: 02 August 2022]

CNEOS has a monitoring system that analyses NEA orbits and computes impact probabilities for potentially hazardous NEAs [7]. Visiting a NEA, especially one with a larger impact probability will allow for more accurate classification and computation of the orbit, and thus allowing for longer preparation time if an asteroid is found to be Earth-bound.

Beyond scientific research and planetary defence, the use of asteroids for space mining and similar extraction of resources in the solar system can alleviate the issues with shortages and limitations on the Earth. Asteroids, especially NEAs, that are rich in resources that may be sought-after on Earth could be mined for their materials and then the resources transported back to Earth. There are a large number of steps required in the selection, set-up, and operation of a terrestrial mine, and these are present for space mining too. The exploratory phase involves determination of the location and dispersion of the desired resource, as well as the logistics of access and operation [8]. Performing a fly-by of a NEA allows for a more accurate classification of the constituent materials of the asteroid which is necessary for the exploratory phase.

1.1.2. Co-Orbital Asteroid Characteristics

The definition of co-orbital asteroids varies slightly among research papers and books. The classification can be asteroid and case-dependent. Marcos and Marcos have carried out a vast amount of research into the subject of co-orbital asteroids (see [9–12]). They define a co-orbital asteroid as one with an orbital period of between 362 and 368 days [13] which equates to a co-orbital zone of ~ 0.994 AU to ~ 1.006 AU. NASA's JPL small body database (SBDB)[2] provides accurate orbital properties and ephemerides for small bodies (asteroids, comets, etc.) in the solar system. A list of 63 asteroids, and their Kepler elements in the Sun-centered J2000 inertial reference frame, that meet the orbital period criteria can be accessed through the SBDB, and the study in this paper is limited to these asteroids. This list can be seen in tabular form in the appendix of the journal article in chapter 2.

Co-orbital objects share a 1:1 mean motion resonance with each other as they orbit a common central object, i.e. both objects complete one orbit about the central body in the same length of time [13]. This means that both objects share a very similar semi-major axis, a. Earth's co-orbital asteroids are a subset of NEAs which follow a co-orbital configuration with Earth. There are three main co-orbital NEA configurations, which are dependant on the mean longitude difference between the asteroid and the planet, ϕ, defined by Brasser et al. [14] as

$$\phi = \lambda_a - \lambda_p \tag{1.1}$$

where λ_a is the mean longitude of the asteroid and λ_p is the mean longitude of the planet.

The most well-known type of co-orbital objects are Trojan asteroids which follow the tadpole (TP) orbits seen in Figure 1.1. Tadpole orbits are defined where ϕ librates around $\phi = \pm 60°$, which is around either the L_4 or L_5 Lagrange point [15]. There are 23 co-orbital NEAs in tadpole orbits.

Horseshoe (HS) orbits librate around $\phi = 180°$, and the grey line in Figure 1.1 shows a possible horseshoe orbit in a Sun-Planet synodic reference frame. There are 13 co-orbital NEAs following horseshoe orbits.

The final type of co-orbital asteroid is known as a quasi-satellite (QS), where the asteroid appears to orbit the planet in retrograde motion, but is not gravitationally-bound to the planet [10]. The motion of a co-orbital asteroid in a quasi-satellite configuration is shown as the red contour in Figure 1.1. The object orbits outside the planet's Hill sphere or sphere of influence and the trajectory of the asteroid will never cross the Hill sphere of the planet [16]. A quasi-satellite typically orbits with a larger eccentricity than the planet, and the mean longitude difference librates around $\phi = 0°$. There are 27 co-orbital NEAs in quasi-satellite configuration about the Earth.

Similar to all NEAs, co-orbital asteroids can give insight on the history and development of the solar system. Theories around the Jovian Trojan satellites originally suggested that they formed alongside Jupiter at similar heliocentric distances, but more recent theories suggest they may have formed over a wider range of distances [18]. Studies of the co-orbital asteroids of Earth may uncover details around their origin, similar to the study of Jupiter's Trojan asteroids. This may give further insight into the conditions during the formation of the solar system, and potentially the components that were present during the formation of life on Earth.

---

[2] Jet Propulsion Laboratory. Small Body Database. Available at `https://ssd.jpl.nasa.gov/horizons/` [Access Date: 13 June 2022]

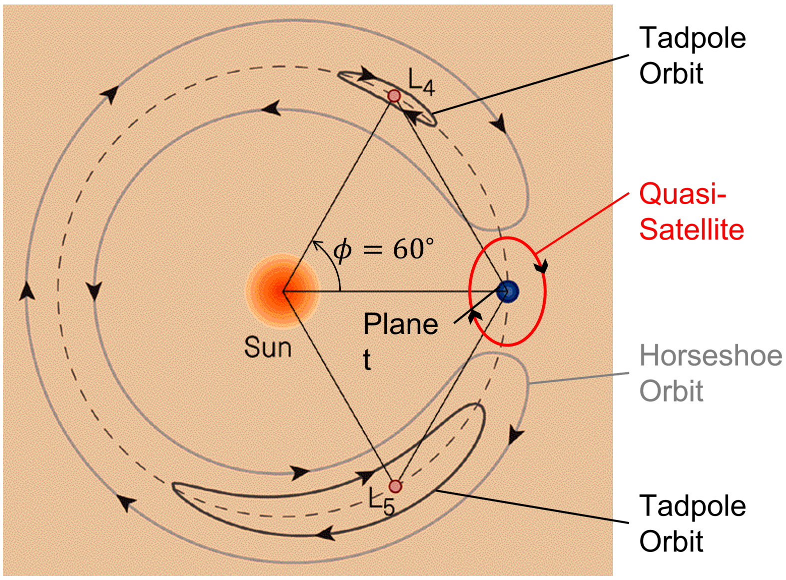

Figure 1.1: Co-orbital asteroid contours. Adapted from [17]

1.2. Solar Sailing

Solar sails have become increasingly popular due to their continuous and endless thrust generation capabilities. By reflecting incident photons from the Sun off a highly reflective surface known as the sail, a thrust is generated [19, 20]. These sails can be maneuvered relative to the incident sunlight in order to control the direction in which the thrust of the spacecraft will act. Contrary to traditional propulsion methods, solar sails require no propellant to generate thrust which can make them lighter and longer-lasting in comparison, depending on the sail size and structure mass. This can lead to a decrease in mission costs due to the lack of propellant needed. Further, solar sailing can be used to create trajectories that have previously been deemed infeasible or difficult, such as high-inclination orbits about the Sun, or displaced orbits high above the ecliptic plane [19].

The theoretical basis of light exerting a pressure was experimentally proven in 1901 [21], which is the theory on which solar sailing is based, but it was not until the 1970s that solar sail mission concepts were seriously explored or considered. Further, the first mission to implement and fully test solar sailing was the Japan Aerospace Exploration Agency (JAXA) Interplanetary Kite-craft Accelerated by Radiation Of the Sun (IKAROS) mission, which launched in 2010 [22, 23]. Later in 2010, the NASA launched NanoSAIL-D2, and this deployed a solar sail from its CubeSat structure in 2011 [24]. *The Planetary Society* have launched two solar sailing missions - LightSail 1 in 2015 and LightSail 2 in 2019 [25, 26]. NASA's NEA Scout and Advanced Composite Solar Sail System (ACS3) are upcoming planned missions to implement and test solar sailing [27, 28].

NEA Scout is the first planned solar sail mission to visit a NEA [27], however there have been a wide range of conceptual missions designed that use various types of solar sailing to visit NEAs. In particular, Heiligers et al. [29] designed a solar sailing mission to asteroid 2016 HO$_3$, which is a co-orbital quasi-satellite of Earth. While the mission design of that paper focused on a visit to a single asteroid, the thesis research presented here will focus on developing a trajectory to visit multiple co-orbital NEAs. A team from the University of Tokyo and JAXA designed a return mission from the Sun-Earth L$_2$ point to a NEA [30]. Similar to the mission designed from L$_2$, trajectories to observe multiple NEAs in one flight using solar sailing have been analysed [31, 32].

The introduction of solar sailing acceleration to a mission allows surfaces of equilibria beyond the five classical Lagrange points to exist. Equilibrium points that lie along the line between the Sun and classical Lagrange points are referred to as sub-Lagrange points, and are denoted as SL$_1$ through SL$_5$. In particular, the sub-Lagrange points SL$_1$ and SL$_2$ are investigated in this thesis as the possible starting locations of the trajectory. It is assumed that the solar sailing spacecraft will take a ride share to either of these equilibrium points, and the full trajectory design begins at either equilibrium point.

The work in this thesis will focus on furthering the research around the development of solar sailing missions to co-orbital NEAs, and builds on previous publications in this area. To date there has not been a theoretical mission designed to multiple co-orbital near-Earth asteroids. The mission developed in this thesis is the first to use solar sailing to visit multiple co-orbital near-Earth asteroids in a single mission.

1.3. Research Objectives

Sections 1.1 and 1.2 outline the relevancy of visiting co-orbital near-Earth asteroids, and the potential role that solar sailing can play in visiting these asteroids. Based on these descriptions, and the findings of the Literature Study [33], the focus of this thesis will be on finding and optimising solar sail trajectories that visit sequences of co-orbital near-Earth asteroids. Thus, the following research objective, which will guide the thesis work, has been formulated:

> To find time- and encounter-optimal solar sailing trajectories to multiple co-orbital near-Earth asteroids.

The objective of this research is to develop solar sailing trajectories to visit as many co-orbital near-Earth asteroids in as short a time period as possible.

The achieving of this objective is supported by the following research questions:

1. Can solar sailing be used as a propulsion method to visit multiple co-orbital asteroids in a given mission length, and if so, how many asteroids can be visited?
2. Which of the co-linear artificial Lagrange points, SL_1 or SL_2, provides an initial position for more optimal trajectories?
3. How do the relative fly-by distances and velocities compare for a fixed-angle control law and an optimised control law?

1.4. Report Structure

The research objective and related questions outlined in section 1.3 will be addressed in chapter 2, which is the main section of the thesis report. This chapter is written in the format of a journal article, specifically the format of the American Institute of Aeronautics and Astronautics (AIAA). Writing the main body of the thesis in this form allows the thesis work to be readily submitted to this journal. The journal article is titled *Solar Sailing Trajectory Design to Multiple Co-Orbital Near-Earth Asteroids*.

This article begins with another abstract and introduction in Section I, which are more condensed than those present in the thesis report itself. Following this, the dynamical model used in the research is introduced in Section II, and an explanation of the target asteroids and the conversion of their ephemerides is provided in Section III. Section IV defines the problem being investigated and some related decisions and assumptions. The method that has been developed to generate initial sequences of asteroids to target is described in Section V, which ends with a description of the chosen initial trajectory. Section VI describes the optimisation of the first leg of this trajectory, first with the definition of the optimal control problem of the thesis, then presenting the results of the optimisation. Finally, Section VII contains the conclusions of the results of the research.

Following the journal article, chapter 3 contains the discussion and conclusion of the results found in the article. In this chapter, the research questions will be addressed and some recommendations will be put forward for work that can follow the findings of this research. Subsequently, Appendix A presents the verification and validation of the dynamical models and numerical techniques that have been utilised during this research.

2

Journal Article

Solar Sailing Trajectory Design to Multiple Co-Orbital Near-Earth Asteroids

Cian Buckley[*]
Faculty of Aerospace Engineering, Delft University of Technology, Kluyverweg 1, 2629HS Delft, The Netherlands

This paper investigates the use of solar sailing propulsion to visit as many co-orbital near-Earth asteroids (NEAs) as possible, within a fixed time-frame. This research builds on previous publications, which have shown solar sailing to be a suitable propulsion method to visit NEAs. The dynamics of this problem are modelled within the Solar Sail Augmented Circular Restricted Three-Body Problem (CR3BPS), and assume a near-term solar sailing technology level. A sequence generation algorithm is developed which generates trajectories to visit multiple co-orbital NEAs beginning at either the artificial co-linear equilibrium point SL$_1$ or SL$_2$. This algorithm develops trajectories with fixed controls to transfer between target asteroids, using Monte Carlo simulations to propagate a wide range of random combinations of settings before selecting those that perform the best. It is shown that the tuning performed within this research can generate a trajectory that enables 18 asteroid fly-bys within the selected nominal mission lifetime of ten years. Following this sequence generation, the first fly-by of the trajectory is optimised as proof of concept that each leg of the trajectory can be optimised for fly-by distance and velocity. An optimal control problem is developed, which is then implemented and solved using direct pseudospectral methods. The solution to this optimal control problem reduces the fly-by distance by 99.95 %, down to 158.73 km, while reducing the fly-by velocity by 9.68 % to 4.33 km/s.

Nomenclature

Latin Symbols

a = Semi-major axis

$\boldsymbol{a}_s$ = acceleration vector within $C(x,y,z)$

$\bar{\boldsymbol{A}}$ = Jacobian Matrix

$C(x,y,z)$ = Synodic Sun-(Earth+Moon) reference frame

t = Time

T = Orbital period

U = Effective potential

$\boldsymbol{u}(t)$ = Control vector of the spacecraft

V = Gravitational potential

---

[*] Graduate Student, Faculty of Aerospace Engineering,`c.p.buckley@student.tudelft.nl`

e = eccentricity

E = Eccentric anomaly

E_{AST} = Individual asteroid encounter

$\boldsymbol{h}$ = Decision variables vector

$\bar{\boldsymbol{I}}$ = Identity matrix

J = Objective function

m = Mass of small body

m_1, m_2 = Mass of primary bodies

M = Mean anomaly

$\bar{\boldsymbol{M}}$ = Gravity gradient matrix

n = Mean motion of the Earth

$\hat{\boldsymbol{n}}$ = Unit vector normal to sail surface

$\bar{\boldsymbol{N}}$ = Radiation gradient matrix

$\boldsymbol{r}$ = Position vector within C(x,y,z)

$\boldsymbol{r}_1, \boldsymbol{r}_2$ = Position vectors relative to m_1, m_2

Δr = Relative distance between spacecraft and target asteroid

$\bar{\boldsymbol{R}}$ = Rotation matrix

$S(\hat{\boldsymbol{r}}_1, \hat{\boldsymbol{p}}, \hat{\boldsymbol{q}})$ = Sail-centered reference frame

Δv = Relative velocity between spacecraft and target asteroid

$\boldsymbol{x}$ = State vector of spacecraft within $C(x, y, z)$

$\boldsymbol{x}(t)$ = State vector of the spacecraft at time t

$\bar{\mathbf{0}}$ = Zero Matrix

Greek Symbols

α = Cone angle

$\tilde{\alpha}$ = Real part of eigenvalue

β = Lightness number

$\tilde{\beta}$ = Imaginary part of eigenvalue

δ = Clock angle

ϵ = Small perturbation

γ = Eigenvalues

μ = Mass ratio

Ω = Right ascension of the ascending node

ω = Argument of periapsis

ψ = Rotation angle

θ = True anomaly

ζ = Eigenvector

I. Introduction

Solar sailing is a method of spacecraft propulsion that uses large reflective surfaces known as sails to generate a thrust from incident solar radiation pressure (SRP). As a concept it is not a new idea, however, its implementation has only become possible in the last number of years due to advancements in technology. The Japan Aerospace Exploration Agency (JAXA) Interplanetary Kite-craft Accelerated by Radiation Of the Sun (IKAROS) mission was the first mission to fully implement and test solar sailing when it was launched in 2010 [1, 2]. Later in 2010, the National Aeronautics and Space Administration (NASA) launched NanoSAIL-D2, and this deployed a solar sail from its CubeSat structure in 2011 [3]. *The Planetary Society* have launched two solar sailing missions - LightSail 1 in 2015 and LightSail 2 in 2019 [4, 5]. NASA's near-Earth Asteroid Scout (NEA Scout) is a mission due to launch in late 2022, which will utilise solar sailing to visit a near-Earth asteroid [6]. NASA's Advanced Composite Solar Sail System (ACS3) mission will test new solar sailing technology, and is planned for launch in 2023 [7]. Many other mission concepts utilising solar sailing have been developed (e.g. see [8–13]), demonstrating the interest in this technology and the potential it holds.

As of August 2022, there are more than 29,000 near-Earth asteroids (NEAs) that have been discovered and characterised by NASA's Jet Propulsion Laboratory (JPL) Center for Near Earth Object Studies (CNEOS)*. There are a wide range of motivations to visit these NEAs. Analysis of the composition and materials of these asteroids can uncover more details surrounding the formation of the Earth and the solar system, including the conditions during formation and the materials present [14]. Planetary defence is another reason for detailed analysis and classification of near-Earth asteroids. If an asteroid is on a trajectory that could impact Earth, the damage could be catastrophic, and the determination of asteroid trajectories in more detail allows further advance warning and thus mitigation strategies. Further, space mining could be a future solution to shortages of materials on Earth, and knowledge around the composition of asteroids is key to select targets for this mining [15]. There have been a number of previous missions to near-Earth asteroids, including both fly-bys and sample return missions [16–23].

Co-orbital asteroids are a subset of near-Earth asteroids that share a 1:1 mean motion resonance with Earth, and are described as having a period of between 362 and 368 days [24]. These asteroids can take the form of tadpole orbits (TP), horseshoe orbits (HS), or quasi-satellites (QS). Similar to near-Earth asteroids, co-orbital asteroids can give insight into the history and development of the Earth and solar system. Co-orbital asteroids of Earth are relatively easy to access from our planet, which makes them interesting and attractive targets for in-situ analysis [25] or sample return missions [26]. Co-orbital NEAs also have an increased probability of becoming Earth impactors, so further classification and analysis can aid in future planetary defense efforts [27]. To date there have been 63 discovered NEAs that fall under the definition of a co-orbital NEA† - 23 co-orbital asteroids in tadpole orbits, 13 in horseshoe orbits, and 27 quasi-satellites.

NEA Scout is the first planned solar sail mission to visit a NEA [6], however there have been a wide range of concepts missions designed that use various types of solar sailing to visit NEAs. In particular, Heiligers et al. [28] designed a solar sailing mission to asteroid 2016 HO_3, which is a co-orbital quasi-satellite of Earth. A team from the University of Tokyo and JAXA designed a return mission from the Sun-Earth L_2 point to a NEA [29]. Trajectories to observe multiple NEAs in one flight using solar sailing have been analysed [30, 31]. The research carried out in this paper aims to complement and build on these previous publications. To date there has not been a theoretical mission designed to multiple co-orbital near-Earth asteroids. The mission developed in this paper is the first to use solar sailing to visit multiple co-orbital near-Earth asteroids in a single mission.

In particular, the objective of the research in this paper is to find a trajectory that visits as many near-Earth co-orbital asteroids as possible, in a fixed time-frame, using only a solar sail as the propulsion method. The dynamics of the

---

*Jet Propulsion Laboratory. CNEOS Discovery Statistics. Available at `https://cneos.jpl.nasa.gov/stats/totals.html`. [Access Date: 02 August 2022]

†Jet Propulsion Laboratory. Small Body Database. Available at `https://ssd.jpl.nasa.gov/horizons/` [Access Date: 13 June 2022]

spacecraft are modelled within the Sun-(Earth+Moon) Solar Sail Augmented Circular Restricted Three-Body Problem (CR3BPS). While the traditional Circular Restricted Three-Body Problem (CR3BP) exhibits five equilibrium points, the introduction of a solar sail acceleration allows equilibria to exist beyond these five locations. Utilised in this research are the artificial sub-Lagrange equilibrium points, SL_1 and SL_2, which exist in the vicinity of the traditional L_1 and L_2 Lagrange points, but are located closer to the Sun due to the additional solar sail acceleration. The spacecraft is assumed to take a ride-share to either the SL_1 or SL_2 Artificial Equilibrium Point (AEP), at which stage the sail will deploy and the spacecraft's motion will only be influenced by SRP acting on the sail. A sequence generation algorithm is developed which generates sequences of asteroids to visit. Starting at either the SL_1 or SL_2 point, a trajectory with fixed angles with respect to the incident sunlight is generated to travel to a co-orbital NEA. From this first asteroid, another trajectory is generated to travel to a second asteroid. This process is then repeated to generate a sequence of asteroids until a nominal mission lifetime is reached. Following the generation of a sequence of asteroids to visit, the first asteroid fly-by is optimised as a proof-of-concept that the generated sequence can be optimised to reduce relative fly-by distance and velocity. While the initial sequence generation focuses solely on finding trajectories that fly as close to asteroids as possible, the optimisation also focuses on reducing the relative velocity between the asteroid and the spacecraft.

This paper is organised as follows. Section II introduces the dynamical model used to represent the solar sailing motion. Following this, Section III discusses the target co-orbital asteroids and the conversion of their ephemerides into the Sun-(Earth+Moon) synodic reference frame. The problem is fully defined in Section IV, before the method of generating the sequence of asteroids to visit is fully developed in Section V. Optimisation of the first leg of this trajectory, including the optimal control problem, is developed in Section VI. Finally, conclusions on the results of the sequence generation and optimisation are discussed in Section VII. The appendix of the paper contains a table of the target asteroids selected for analysis in this research, and a flowchart for the process of selecting the sequences of asteroids to visit.

II. Dynamics

This section presents the models used in the paper's investigation, namely, the CR3BPS and solar sail steering. The equilibrium points within the CR3BPS and an analysis of their stability are also discussed. The target asteroids selected for this mission all have orbits in relative proximity to the Earth and will not approach any other bodies in the solar system in their near-term predicted orbits. Similarly, the gravitational acceleration of the Earth-Moon system and the Sun are the main gravitational forces acting on the spacecraft. The eccentricity, e, of the orbit of the Earth around the Sun is very close to zero ($e = 0.016710$ [32]), and for the purpose of this research is assumed to be zero. Due to the relative proximity of the target asteroids and the solar sailing spacecraft to the Earth and Moon, the dynamical framework chosen to represent this problem is the Sun-(Earth+Moon) CR3BPS, where the Earth-Moon system is assumed to be a single body. The CR3BPS has been extensively used in previous solar sailing mission design, see e.g., [9, 28, 33].

A. Acceleration Model

The CR3BP describes the motion of an infinitesimally small body, m, under the gravitational influence of two primary bodies, m_1 and m_2, which orbit their common center-of-mass in perfect circles [34]. A schematic of the CR3BP can be seen in Figure 1. In this paper the primary body, m_1, is the Sun, the primary body, m_2, is the Earth-Moon system, and the third body, m, is the solar sailing spacecraft. The reference frame selected to define the dynamics of the spacecraft and the asteroids is the synodic Sun-(Earth+Moon) reference frame $C(x, y, z)$. The frame $C(x, y, z)$ is centered on the Sun-(Earth+Moon) barycenter, with the $x-$axis pointing towards the center of mass of the Earth+Moon system, the $z-$axis perpendicular to the orbital plane of the Earth+Moon system about the Sun, and the $y-$axis completes the right-handed reference frame. The $C(x, y, z)$ reference frame rotates at a constant angular velocity, ω, around the z-axis.

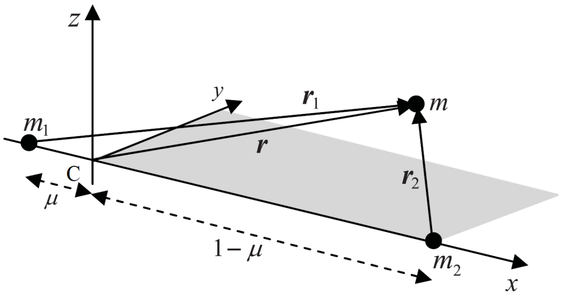

Fig. 1 Schematic of the circular restricted three-body problem (adapted from Heiligers et al. [28]).

The units of mass, distance, and time are normalized in the CR3BP. The unit of mass is taken as the total mass of the system, i.e. $m_1 + m_2 = 1$. Introducing the mass ratio $\mu = \frac{m_2}{m_1+m_2}$, the masses of the Sun and Earth-Moon system become $m_1 = 1 - \mu$ and $m_2 = \mu$, respectively. In this paper, the mass ratio is taken as $\mu = 3.04086372908 \times 10^{-6}$ [‡]. The unit of distance is taken as the distance between the Sun and the Earth-Moon system (1 AU, 149.5979×10^9 m [32]), while the unit of time is the inverse of the rotational angular velocity $\frac{1}{\omega}$. Thus, one revolution of the reference frame (i.e. one year) is given by 2π.

The motion of a body within the synodic reference frame, with the assumptions introduced previously, is described by [28]

$$\ddot{\boldsymbol{r}} + 2\boldsymbol{\omega} \times \dot{\boldsymbol{r}} + \boldsymbol{\omega} \times (\boldsymbol{\omega} \times \boldsymbol{r}) = \boldsymbol{a}_s - \nabla V \tag{1}$$

where $\boldsymbol{r} = [x,\ y,\ z]^T$ is the position vector of the spacecraft m in the synodic reference frame $C(x, y, z)$, $\boldsymbol{\omega} = [0,\ 0,\ 1]^T$

[‡] $m_{Earth} = 5.9736 \times 10^{24}$ kg, $m_{Moon} = 7.348 \times 10^{22}$ kg, $m_{Sun} = 1.9886 \times 10^{30}$ [32].

is the angular velocity vector of the reference frame, $\boldsymbol{a}_s$ is the acceleration of the spacecraft due to the solar sail, and V is the gravitational potential given by

$$V = -\left(\frac{1-\mu}{r_1} + \frac{\mu}{r_2}\right) \tag{2}$$

where r_1 and r_2 are the magnitudes of the position vectors of the spacecraft relative to the Sun and Earth-Moon system respectively: $\boldsymbol{r}_1 = [x+\mu,\ y,\ z]^T$, $\boldsymbol{r}_2 = [x-(1-\mu),\ y,\ z]^T$ as can be seen in Figure 1.

Introducing an effective potential U, the system can be rewritten as

$$\ddot{\boldsymbol{r}} + 2\omega \times \boldsymbol{r} = \boldsymbol{a}_s - \nabla U \tag{3}$$

where the effective potential U is given by

$$U = -\left(\frac{1-\mu}{r_1} + \frac{\mu}{r_2}\right) - \frac{1}{2}\left(x^2 + y^2\right) \tag{4}$$

In this study, the solar sail model assumed is an ideal sail, which is perfectly flat with perfect specular reflection of the incident photons. This model neglects any effects of absorption, diffuse reflection, thermal emission, or wrinkling [35, 36]. For an ideal solar sail, in the dimensionless units introduced previously, the acceleration due to SRP acting on the sail $\boldsymbol{a}_s$ is given by [35]

$$\boldsymbol{a}_s = \beta \frac{1-\mu}{r_1^2} \left(\hat{\boldsymbol{r}}_1 \cdot \hat{\boldsymbol{n}}\right)^2 \hat{\boldsymbol{n}} \tag{5}$$

where β is the lightness number of the solar sail, which is a measure of the effectiveness of the sail, and $\hat{\boldsymbol{n}}$ is the unit vector normal to the surface of the solar sail, so the acceleration acts perpendicular to the sail surface.

The lightness number, β, is a function of the sail area to spacecraft mass ratio, and can also be defined as the ratio of solar radiation pressure acceleration to solar gravitational acceleration [10, 37, 38]. Values for the lightness numbers of previous missions, and the predicted lightness numbers of upcoming missions, are tabulated in Table 1. Near-term predicted technology levels for solar sailing are expected to allow lightness number of up to $\beta = 0.04$ [39].

Mission	Lightness Number β
IKAROS	~ 0.001 [9]
NanoSAIL-D2	0.00385 [9]
LightSail 2	0.0098 [5]
NEA Scout	~ 0.01 (predicted) [39]
ACS3	~ 0.01 (predicted) [39]

Table 1 Past and predicted lightness number, β, values of solar sailing missions.

B. Solar Sail Steering

The acceleration due to the SRP acting on the solar sail is dependent on the orientation of the sail, as can be seen from the normal component $\hat{\boldsymbol{n}}$ in Eq. 5 and in Figure 2. This normal vector determines both the direction and magnitude of the acceleration of the spacecraft due to solar sailing. The normal vector can be defined through two angles - the cone and clock angles, α and δ, respectively. These angles define the solar sail's orientation relative to the direction of sunlight, which is directed along the Sun-sail line $\hat{\boldsymbol{r}}_1$. A new reference frame $S(\hat{\boldsymbol{r}}_1, \hat{\boldsymbol{p}}, \hat{\boldsymbol{q}})$ can be defined in which to define the cone and clock angles. The two remaining axes are defined as in Figure 2: $\hat{\boldsymbol{p}} = \hat{\boldsymbol{z}} \times \hat{\boldsymbol{r}}_1$ and $\hat{\boldsymbol{q}} = \hat{\boldsymbol{r}}_1 \times \hat{\boldsymbol{p}}$. The cone angle is the angle between the normal vector $\hat{\boldsymbol{n}}$ and the Sun-sail vector $\hat{\boldsymbol{r}}_1$, while the clock angle is the angle between the projection of $\hat{\boldsymbol{n}}$ onto the $(\hat{\boldsymbol{p}}, \hat{\boldsymbol{q}})$-plane and $\hat{\boldsymbol{q}}$. Thus, the sail orientation can be defined within frame $S(\hat{\boldsymbol{r}}_1, \hat{\boldsymbol{p}}, \hat{\boldsymbol{q}})$ as [35]

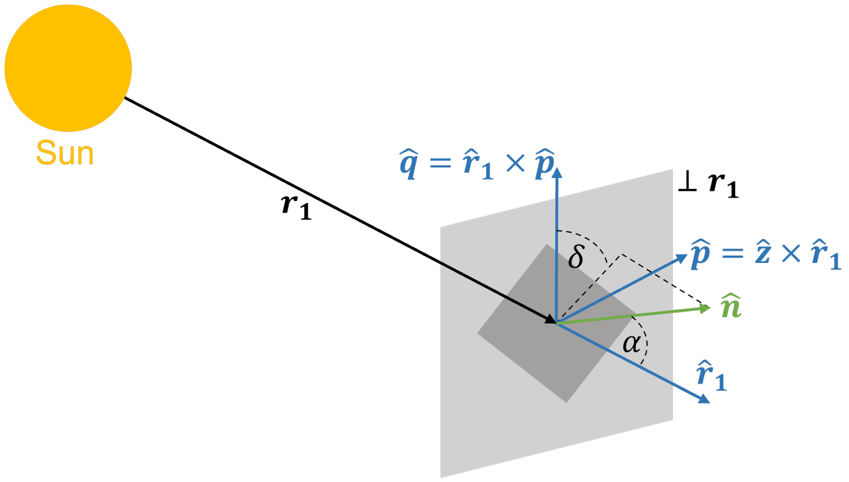

Fig. 2 Solar sail cone and clock angles as defined in reference frame $S(\hat{\boldsymbol{r}}_1, \hat{\boldsymbol{p}}, \hat{\boldsymbol{q}})$.

$$\hat{\boldsymbol{n}}|_S = \begin{bmatrix} \cos\alpha \\ \sin\alpha\sin\delta \\ \sin\alpha\cos\delta \end{bmatrix} \tag{6}$$

The unit normal vector $\hat{\boldsymbol{n}}$ cannot point towards the Sun, as this would imply an acceleration in the direction of the Sun due to SRP. Therefore $(\hat{\boldsymbol{r}}_1 \cdot \hat{\boldsymbol{n}}) = \cos\alpha \geq 0$, which implies that $\alpha \in [-\frac{\pi}{2}, \frac{\pi}{2}]$ [8]. The clock angle can take values of $\delta \in [0, \pi]$ which ensures that $\hat{\boldsymbol{n}}$ can point in all possible directions away from the Sun.

Through a reference frame transformation matrix, the normal vector $\hat{\boldsymbol{n}}$ can be transformed from the sail-centered reference frame $S(\hat{\boldsymbol{r}}_1, \hat{\boldsymbol{p}}, \hat{\boldsymbol{q}})$ to the Sun-(Earth+Moon) synodic reference frame $C(x, y, z)$ through

$$\hat{\boldsymbol{n}} = \hat{\boldsymbol{n}}|_C = [\hat{\boldsymbol{r}}_1 \ \hat{\boldsymbol{p}} \ \hat{\boldsymbol{q}}]\hat{\boldsymbol{n}}|_S \tag{7}$$

C. Equilibrium Points

Equilibrium points are stationary solutions to systems of differential equations. For the CR3BPS, the equilibrium points are locations in the $C(x, y, z)$ frame where a solar sailing object placed at rest will remain at rest. No net acceleration will act on a body placed, with no velocity, at one of these points, i.e. $\ddot{\boldsymbol{r}} = \dot{\boldsymbol{r}} = 0$. Substituting these conditions into Eq. 3 allows the location of equilibrium points in the CR3BPS to be found through

$$\nabla U = \boldsymbol{a}_s = \beta \frac{1-\mu}{r_1^2} \left(\hat{\boldsymbol{r}}_1 \cdot \hat{\boldsymbol{n}}\right)^2 \hat{\boldsymbol{n}} \tag{8}$$

For a body where the SRP acting on it is negligible (i.e. $\beta = 0$), Eq. 8 can be simplified to $\nabla U = 0$. Solving this equation allows for the five classical, well-known equilibrium points to be found. These points are known as Lagrange points, as they were first discovered by Lagrange in 1772 [34].

The introduction of a solar sail acceleration into the dynamical model allows surfaces of artificial equilibria, known as AEPs, to exist. The locations of these AEPs can be found by solving Eq. 8, which can only be satisfied if ∇U acts in the same direction as the sail normal $\hat{\boldsymbol{n}}$. This imposes a constraint on the required solar sail orientation, which can be found through $\hat{\boldsymbol{n}} = \frac{\nabla U}{|\nabla U|}$. Taking the dot product of both sides of Eq. 8 with $\hat{\boldsymbol{n}}$ and rearranging, the required lightness number for an AEP to exist can be calculated as follows [35]

$$\beta = \frac{r_1^2}{1-\mu} \frac{\nabla U \cdot \hat{\boldsymbol{n}}}{\left(\hat{\boldsymbol{r}}_1 \cdot \hat{\boldsymbol{n}}\right)^2} \tag{9}$$

AEPs that lie along the line between the Sun and the traditional Lagrange points are referred to as sub-Lagrange points, and are denoted as SL_1 through SL_5. The x-coordinates of the SL_1 and SL_2 for $\beta = 0.04$ are given in Table 2.

Point	**x-coordinate**
SL_1	0.98298982
SL_2	1.00708364

Table 2 SL_1 and SL_2 x-coordinates for $\beta = 0.04$.

D. Stability of Equilibria

An equilibrium point can be considered stable if the motion of the body remains bounded to the vicinity of the equilibrium point when a small displacement or perturbation is imposed upon the body. The stability of an equilibrium point can be analysed numerically by linearising the system around the equilibrium point and finding the Jacobian matrix, $\bar{\boldsymbol{A}}$, of this linearised system, where the Jacobian is defined as [35, 40]

$$\bar{\boldsymbol{A}} = \begin{bmatrix} \bar{\mathbf{0}} & \bar{\boldsymbol{I}} \\ \bar{\boldsymbol{N}} - \bar{\boldsymbol{M}} & 2\bar{\boldsymbol{\theta}} \end{bmatrix}; \quad \bar{\boldsymbol{\theta}} = \begin{bmatrix} 0 & 1 & 0 \\ -1 & 0 & 0 \\ 0 & 0 & 0 \end{bmatrix} \tag{10}$$

where $\bar{\mathbf{0}}$ denotes a 3×3 zero matrix, $\bar{\boldsymbol{I}}$ is a 3×3 identity matrix, and $\bar{\boldsymbol{N}}$ and $\bar{\boldsymbol{M}}$ are the radiation and gravity gradient matrices respectively [35], as given by

$$\bar{\boldsymbol{N}} = \begin{bmatrix} a_{xx} & a_{xy} & a_{xz} \\ a_{yx} & a_{yy} & a_{yz} \\ a_{zx} & a_{zy} & a_{zz} \end{bmatrix}, \quad \bar{\boldsymbol{M}} = \begin{bmatrix} U_{xx} & U_{xy} & U_{xz} \\ U_{yx} & U_{yy} & U_{yz} \\ U_{zx} & U_{zy} & U_{zz} \end{bmatrix} \tag{11}$$

where, as an example, a_{xy} is the partial derivative of the x component of the solar sail acceleration $\boldsymbol{a}_s$, with respect to y, and U_{xy} is the partial derivative of the x component of the gradient of the effective potential ∇U, with respect to y.

Motion in the vicinity of these equilibrium points depends on the stability of the points, which is given through the eigenvalues

$$\gamma_i = \pm\tilde{\alpha} \pm \tilde{\beta} i \tag{12}$$

where γ_i is an eigenvalue of the Jacobian $\bar{\boldsymbol{A}}$, $\pm\tilde{\alpha}$ is the real part of the eigenvalue, and $\pm\tilde{\beta}i$ is the imaginary part of the eigenvalue.

The co-linear AEPs have eigenvalues given by $\gamma_{1,2} = \pm\tilde{\alpha}$ and $\gamma_{3,4} = \pm\tilde{\beta}i$. Exciting the motion associated with the imaginary eigenvalues, $\gamma_{3,4}$, gives stable periodic motion around the Lagrange points, while exciting the motion associated with the real eigenvalues, $\gamma_{1,2}$, gives unstable motion to or from the Lagrange points, known as invariant manifolds [40]. The eigenvalue associated with the positive real part, $\gamma_2 = +\tilde{\alpha}$, is associated with stable motion towards the Lagrange point, while the eigenvalue associated with the negative real part, $\gamma_1 = -\tilde{\alpha}$, is associated with unstable motion away from the Lagrange point. To model these manifolds, a small perturbation can be applied to the spacecraft's state at an equilibrium point in the direction of the unstable eigenvectors, $\boldsymbol{\zeta}_{1,2}$, which are associated with the eigenvalues, $\gamma_{1,2}$, through

$$\boldsymbol{x}_{0,U} = \boldsymbol{x}_{SL} \pm \epsilon\hat{\boldsymbol{\zeta}}_1 \tag{13a}$$

$$\boldsymbol{x}_{0,S} = \boldsymbol{x}_{SL} \pm \epsilon\hat{\boldsymbol{\zeta}}_2 \tag{13b}$$

where $\boldsymbol{x}_{0,U} = [\boldsymbol{r}\ \dot{\boldsymbol{r}}]^T$ is the initial perturbed state vector of the spacecraft associated with unstable motion, $\boldsymbol{x}_{0,S} = [\boldsymbol{r}\ \dot{\boldsymbol{r}}]^T$ is the initial perturbed state vector of the spacecraft associated with stable motion, $\boldsymbol{x}_{SL}$ is the state vector of the spacecraft at an artificial Lagrange point, ϵ is a small perturbation in the order of 10^{-4} to 10^{-6} [40, 41], $\hat{\boldsymbol{\zeta}}_1$ is a unit eigenvector associated to the negative real eigenvalue, γ_1, and $\hat{\boldsymbol{\zeta}}_2$ is a unit eigenvector associated to the positive real eigenvalue, γ_2.

Stable manifolds towards the equilibrium point can be obtained by integrating the perturbed state, $\boldsymbol{x}_{0,S}$, in Eq. 13b backwards in time, while unstable manifolds away from the equilibrium point can be obtained by integrating the perturbed state, $\boldsymbol{x}_{0,U}$, in Eq. 13a forwards in time. These unstable manifolds can be from either the (S)L$_1$ or (S)L$_2$ (artificial) equilibrium point, and the initial state of the manifold can be perturbed in either the direction of the unstable eigenvector, $\boldsymbol{\zeta}_1$, or opposite the direction of the unstable eigenvector (i.e. $-\boldsymbol{\zeta}_1$). For conciseness, from here on, an initial perturbed state vector in the direction of the eigenvector, i.e. $\boldsymbol{x}_0 = \boldsymbol{x}_{SL} + \epsilon\hat{\boldsymbol{\zeta}}_1$, is referred to as a *positive perturbation*, while an initial perturbed state vector in the direction opposite the eigenvector, i.e. $\boldsymbol{x}_0 = \boldsymbol{x}_{SL} - \epsilon\hat{\boldsymbol{\zeta}}_1$, is referred to as a *negative perturbation*. These unstable manifolds are used as the initial part of the trajectory designed in this paper. The stable and unstable manifolds to and from the artificial equilibrium points, SL$_1$ and SL$_2$, for a solar sail lightness number of $\beta = 0.04$ can be seen in Figure 3. A zoomed view about the Earth and the SL$_2$ point can also be seen in this figure.

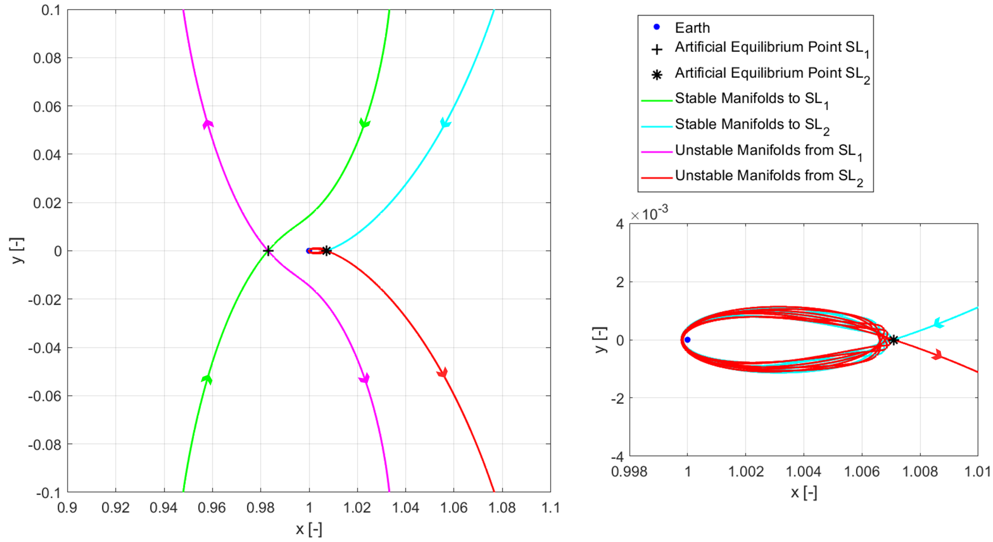

Fig. 3 Stable and unstable manifolds to and from the artificial equilibrium points for a solar sail lightness number of $\beta = 0.04$**.**

III. Target Asteroids

There is no formal quantitative definition of co-orbital asteroids. However, Marcos and Marcos have performed extensive research on co-orbital asteroids and their properties (see [24–26, 42]). They define a co-orbital asteroid as having an orbital period of between 362 and 368 days [24], which equates to a co-orbital semi-major axis range of ~0.994 AU to ~1.006 AU. NASA's JPL Small Body Database (SBDB)[§] provides accurate orbital properties and ephemerides for small bodies (asteroids, comets, etc.) in the solar system. A list of 63 asteroids that meet the orbital period criteria can be accessed through the SBDB, and the study in this paper is limited to these asteroids. There are 23 co-orbital asteroids in tadpole orbits, 13 in horseshoe orbits, and 27 quasi-satellites. The Kepler elements and orbit type of these 63 asteroids in the Sun-centered J2000 inertial reference frame can be found in Table 10 in the Appendix. The J2000 inertial frame, $J(x_J, y_J, z_J)$, is based on the position and motion of the Earth on 1 January 2000 at 12:00 Terrestrial Time. The x_J-axis of this reference frame lies on the vernal equinox, while the z_J-axis is normal to the Earth's spin axis [43]. The y_J-axis completes the right-hand reference frame.

The ephemerides of these co-orbital asteroids are retrieved from the SBDB over a period of 20 years to allow for a range of initial possible launch dates. These ephemerides provide the position and velocity of each asteroid within the $J(x_J, y_J, z_J)$ frame. A time step for each measurement of one day is chosen, as this gives a balance between efficiency of the program and accuracy of the results. These position and velocity vectors are converted into the $C(x, y, z)$ reference frame through a reference frame rotation and translation, as discussed below. This reference frame transformation allows for the trajectory of the solar sail spacecraft to be directly compared to the motion of the target asteroids.

The provided ephemeris files contain the asteroids' states within the J2000 reference frame. The state vector is provided as

$$\boldsymbol{x}_A|_J = [\boldsymbol{r}_A \quad \dot{\boldsymbol{r}}_A]^T \tag{14}$$

This state vector can be converted to the synodic Sun-(Earth+Moon) reference frame through

$$\begin{bmatrix} x \\ y \\ z \end{bmatrix}_{C(x,y,z)} = \bar{\boldsymbol{R}} \begin{bmatrix} x \\ y \\ z \end{bmatrix}_{J(x_J,y_J,z_J)} + \begin{bmatrix} -\mu \\ 0 \\ 0 \end{bmatrix} \tag{15a}$$

$$\begin{bmatrix} \dot{x} \\ \dot{y} \\ \dot{z} \end{bmatrix}_{C(x,y,z)} = \bar{\boldsymbol{R}} \left(\begin{bmatrix} \dot{x} \\ \dot{y} \\ \dot{z} \end{bmatrix}_{J(x_J,y_J,z_J)} + \boldsymbol{\omega} \times \begin{bmatrix} x \\ y \\ z \end{bmatrix}_{J(x_J,y_J,z_J)} \right) \tag{15b}$$

where $\bar{\boldsymbol{R}}$ is a rotation matrix and $\boldsymbol{\omega}$ is the angular velocity vector of the synodic reference frame.

[§] Jet Propulsion Laboratory. Small Body Database. Available at `https://ssd.jpl.nasa.gov/horizons/` [Access Date: 13 June 2022]

The rotation matrix, $\bar{\boldsymbol{R}}$ is calculated through

$$\bar{\boldsymbol{R}} = \begin{bmatrix} \cos\psi & -\sin\psi & 0 \\ \sin\psi & \cos\psi & 0 \\ 0 & 0 & 1 \end{bmatrix} \tag{16}$$

where ψ is the rotation angle and is simply the sum of the right ascension of the ascending node of the Earth, Ω, the argument of periapsis of the Earth, ω, and the instantaneous true anomaly of the Earth, θ, i.e. $\psi = \Omega + \omega + \theta$. For two-body motion, the values of Ω and ω are fixed, and this assumption is valid in this paper due to the assumption that the solar sailing spacecraft exerts no gravitational influence on the two larger masses. Fixed values of $\Omega = 359.9958°$ and $\omega = 104.4542°$ are extracted from the SBDB for the Earth about the Sun at a reference time t_0 at 00:00 on January 1st 2023.

An initial true anomaly at time t_0 of $\theta_0 = 355.6651°$ is taken from the SBDB. Again, due to the assumption of circular motion, the instantaneous true anomaly θ at time t can be calculated based on the time difference since the reference time $(t - t_0)$, and the initial true anomaly as follows [44]

$$\theta = n(t - t_0) + \theta_0 \tag{17}$$

where n is the mean motion as calculated through

$$n = \sqrt{\frac{\mu_S}{a_E^3}} \tag{18}$$

where μ_S is the gravitational constant of the central body (the Sun in this case), and a_E is the semi-major axis of the Earth.

This process is repeated for each time step of the asteroid ephemeris file. These updated target asteroid ephemerides are directly compared to the trajectory of the spacecraft to determine the relative motion.

IV. Problem Definition

This section introduces and defines the problem that is investigated in this paper. The objective of the mission is fully explained, before a set of mission assumptions are introduced, and the methodology with which the problem will be set up and solved is defined.

A. Problem Objective

The objective of this study is to find a spacecraft trajectory to encounter as many co-orbital near-Earth asteroids as possible in a fixed time-frame, using solar radiation pressure on a solar sail as the only source of propulsion. It is assumed that the spacecraft will ride-share with a a larger mission to either the Sun-Earth L_1 or L_2 point, and that the initial position of the spacecraft is either SL_1 or SL_2. Future planned missions to the Sun-Earth Lagrange points include NASA's Interstellar Mapping and Acceleration Probe (IMAP) mission to L_1 in 2025 [45] and ESA's PLAnetary Transits and Oscillations of stars (PLATO) mission to L_2 in 2026 [46]. Based off these planned missions, the initial date at which the spacecraft will leave the the AEP is constrained to a two year window, from January 1st 2025 to December 31st 2026. The nominal mission duration is taken to be ten years. Solar sailing provides theoretically limitless thrust capabilities, and assuming no problems are encountered, the mission could be extended beyond ten years. However, due to the slightly unstable nature of co-orbital asteroids, more uncertainties are introduced to the ephemerides as time progresses. For this reason, the balanced nominal duration of ten years is selected. The lightness number used in this research is selected as $\beta = 0.04$, which is based on near-term estimates for feasible lightness numbers [39].

B. Methodology

A sequence generation algorithm is developed in *MATLAB*$^{(R)}$, which uses Monte Carlo (MC) simulations to generate sequences of fixed-angle trajectories from one asteroid to another. A search space analysis on the first leg of the trajectory is carried out to determine feasible and infeasible cone and clock angles, α and δ, for the beginning of the trajectory. The results from this analysis are implemented into a full initial trajectory development. Some tuning of the developed algorithm for sequence and trajectory generation is carried out. After sufficient tuning, the chosen settings are implemented and an initial trajectory is developed, with a fixed cone and clock angle for each leg. This initial trajectory contains multiple fly-bys of co-orbital near-Earth asteroids within the nominal ten year mission lifetime.

The first fly-by of this initial trajectory is then optimised using PSOPT, which is a C++ implementation of direct pseudospectral methods [47]. This optimisation is performed to investigate whether the trajectory of the spacecraft can be modified to reduce the relative distance and velocity between it and the asteroid. The optimisation is set up in such a way as to not compromise the following legs of the trajectory. Optimising the first fly-by can act as a proof of concept that subsequent fly-bys can be optimised.

V. Initial Trajectory Design

This section describes the development of an algorithm to generate fixed-angle sequential trajectories to multiple co-orbital near-Earth asteroids. This algorithm generates a trajectory that maximises the number of fly-bys of target asteroids within the nominal mission lifetime. These trajectories contain multiple legs, where each leg has a fixed cone angle, α, and a fixed clock angle, δ, referred to as a fixed-angle control law. Each leg brings the spacecraft to the vicinity of a target asteroid, and the leg is terminated when the relative distance between the spacecraft and the asteroid is minimised. There are a number of parameters which can be varied within this algorithm, and these are tested and tuned before a final full trajectory is generated.

A. Objective Function

The objective of this research is to encounter as many co-orbital asteroids as possible within a nominal ten year mission lifetime. The objective function to be maximised, J_0, for the generation of the initial trajectory is thus defined as

$$J_0 = \sum E_{AST} \tag{19}$$

where E_{AST} is an individual asteroid encounter.

After conversion from the inertial $J(x_J, y_J, z_J)$ reference frame to the synodic $C(x, y, z)$ reference frame, the maximum change in position of an asteroid over a single time step is found to be in the region of 10^6 km. Therefore, any asteroid encounter for the initial analysis is assumed to occur when the spacecraft's position is within 5×10^5 km of an asteroid.

In the case that multiple trajectories have the same objective function but comprise of different target asteroids, the optimal trajectory will be selected as the one in which the flight time is minimised.

B. Sequence Generation Algorithm

A flowchart of the operation of the developed algorithm can be seen in Figure 13 in the Appendix, with an explanation of each step in Table 12.

Code is developed in *MATLAB*$^{\text{(R)}}$ to build up a trajectory leg by leg. Each leg is propagated forward for two years using a Runge-Kutta 4(5) integrator implemented through the *ode45.m* function in *MATLAB*$^{\text{(R)}}$. The decision variables for each leg of the algorithm are

$$\boldsymbol{h}_i = [\alpha_i \;\; \delta_i \;\; t_{0,i} \;\; \boldsymbol{x}_{0,i}]^T \tag{20}$$

where i refers to the leg number, α_i and δ_i are the cone and clock angles of the solar sail, $t_{0,i}$ is the initial propagation time, and $\boldsymbol{x}_{0,i}$ is the initial state of the spacecraft.

The cone and clock angles, α and δ, are randomly selected from within their given bounds of $\alpha \in \left[-\frac{\pi}{2},\ \frac{\pi}{2}\right]$, $\delta \in [0,\ \pi]$, and kept constant over the whole leg. For the first leg, the initial time, t_0, is randomly selected from the two year departure window of 1 Jan 2025 to 31 Dec 2026, and the initial state of the spacecraft, $\boldsymbol{x}_0$, is selected as either a positive or negative perturbation from either the SL$_1$ or SL$_2$ artificial equilibrium points For subsequent legs, the initial time is the time at which a fly-by occurred for the previous leg, and the initial state of the spacecraft is the state of the spacecraft when a fly-by occurred on the previous leg, i.e.

$$t_{0,i} = t_{f,i-1} \tag{21a}$$

$$\boldsymbol{x}_{0,i} = \boldsymbol{x}_{f,i-1} \tag{21b}$$

where f refers to the instant a fly-by occurred.

Over these two years the motion of the spacecraft relative to the target asteroids is analysed to determine if the fly-by conditions have been met. The decision variables that give trajectories where fly-by conditions are met are then ranked based on the transfer time to their target asteroid - shorter transfer times are classified as more optimal. A number of these initial legs are then carried forward to the second leg. The initial condition of the second leg is the spacecraft's state at the time step where an asteroid fly-by occurred. Again, cone and clock angles are randomly selected, and the trajectory is propagated forward for a maximum of two years, while the motion relative to the target asteroids is analysed. If no asteroid is encountered, according to the 5×10^5 km threshold, within the leg's two year length, the minimum fly-by distance of all the target asteroids is used to rank the trajectories, and the initial condition for the next leg is taken as the condition at the asteroid where the closest fly-by occurs. This process is repeated until the nominal mission lifetime of ten years is reached.

Constraints are placed on the motion of the spacecraft to ensure its trajectory does not bring it too close to either the Sun or the Earth-Moon system. If the spacecraft ventures too close to either of these bodies, the gravitational acceleration is too strong and the spacecraft is eventually pulled into the body. This trajectory is both inefficient to calculate and provides no possible asteroid fly-bys. For this reason, the propagation of the trajectory of the solar sail spacecraft is terminated if the spacecraft comes within 0.3 AU of the Sun, or 0.005 AU ($\sim 750,000$ km) of the Earth-Moon system. A constraint on the maximum distance from the Sun that the spacecraft can travel is also implemented at 2 AU from the Sun. The orbits of the target asteroids are all well within these constraints, so none are excluded.

The developed algorithm has a number of settings that can be varied, which effect the performance of the algorithm and number of fly-bys that the resulting trajectories contain. Analysis on these settings is performed to determine the combination that gives the most fly-bys in the ten year period. The setting that are tested are the initial state, the random number generation method, the number of previous runs to carry forward to the next leg, and the number of Monte Carlo simulations to perform at each leg. The proportion of runs to carry forward to the next leg is rounded to the next whole number if it does not provide a whole number value.

C. Initial Search Space Analysis

Before the developed code is used to generate a suitable initial trajectory, the search space of the first leg is analysed. This analysis is performed to determine feasible and infeasible initial settings.

A grid search is performed on the initial leg of the trajectory after these terminal conditions are implemented. The cone angle is varied between $\alpha \in \left[-\frac{\pi}{2}, \frac{\pi}{2}\right]$, while the clock angle is varied between $\delta \in [0, \pi]$, each at a resolution of 5°. The results are shown in Figure 4 to Figure 7, where the left plot of each figure shows cone and clock angle combinations that result in early termination of the trajectory, and the plot on the right of each figure shows the range of trajectories that do not terminate early. Note the differing scales for the termination time.

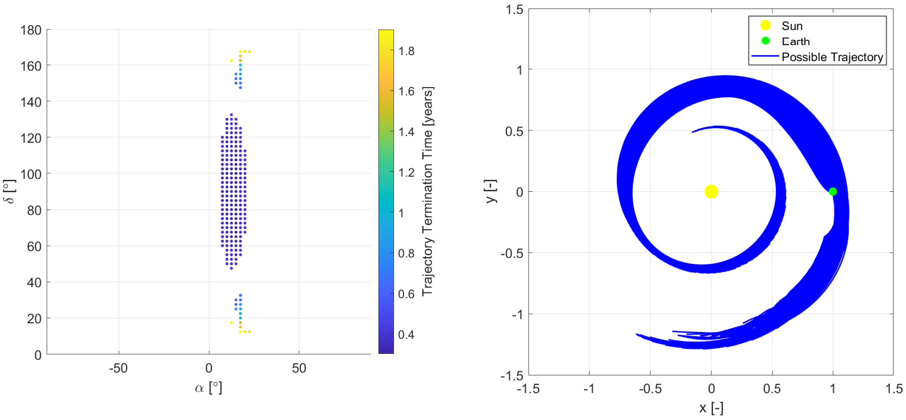

Fig. 4 Search space analysis for the first leg from SL$_1$ with a positive perturbation.

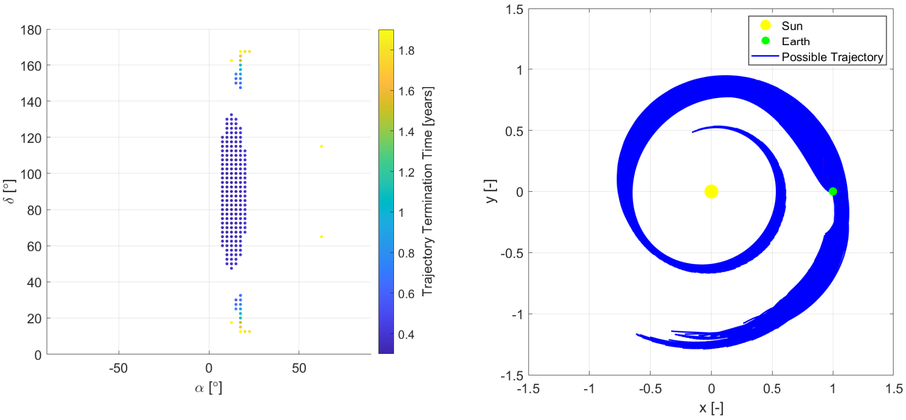

Fig. 5 Search space analysis for the first leg from SL$_1$ with a negative perturbation.

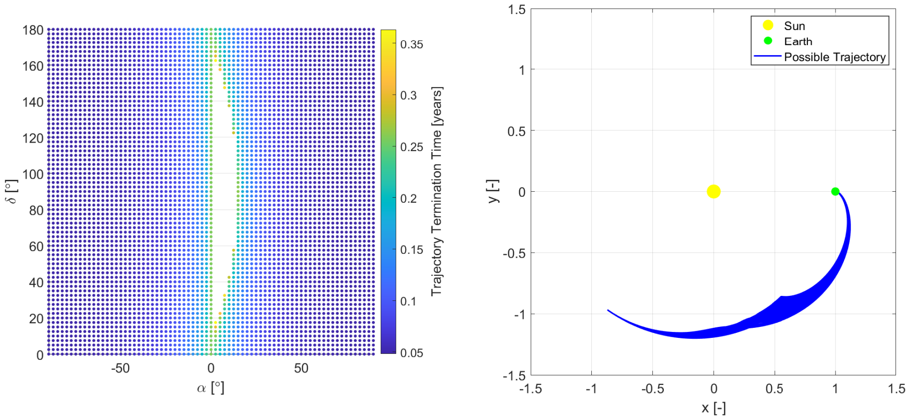

Fig. 6 Search space analysis for the first leg from SL_2 with a positive perturbation.

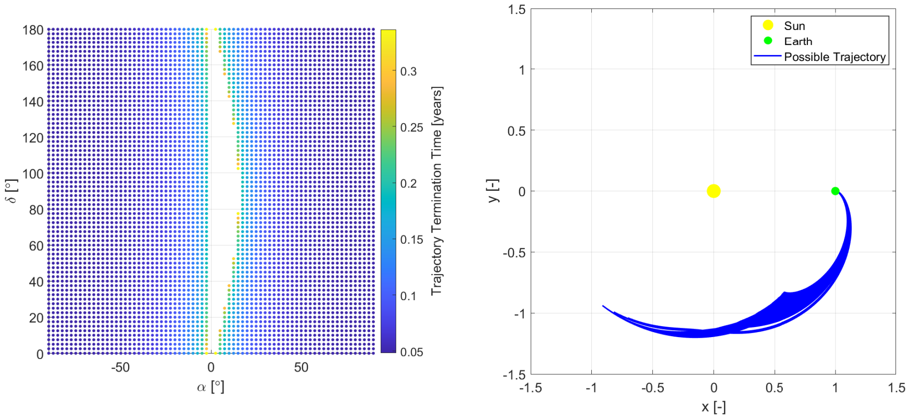

Fig. 7 Search space analysis for the first leg from SL_2 with a negative perturbation.

When comparing these solar sail trajectories to the trajectories of the asteroids within the possible time frame, it appears that there are asteroids that cannot be reached using the fixed-angle control law from any date within the possible range. A list of asteroids that can be encountered from each of these starting conditions is given in Table 11 in the Appendix, where SL_1, + refers to a positive perturbation from SL_1, etc. If an asteroid can not be encountered from the selected starting condition, i.e. there is a *No* in Table 11, the ephemeris of the asteroid are not compared to the trajectory of the spacecraft for the first leg, thus decreasing computational time for the first leg. Similarly, if the randomly generated cone and clock angle combination in the first leg of the sequence is contained in the infeasible combinations found in the grid searches, the algorithm generates a new combination until the trajectory does not terminate early.

Further, it is determined that a positive perturbation from SL_1 can reach more asteroids than a negative perturbation, and a negative perturbation from SL_1 can not reach any asteroids that are not reached through a positive perturbation, i.e., the set of asteroids reached from a negative SL_1 perturbation is a subset of those reached from a positive SL_1 perturbation. The opposite is true for SL_2, with the targets reached from a positive perturbation being a subset of the targets reached through a negative perturbation. This leads to a reduction in the initial conditions that are implemented from four to two. The possible initial conditions can be seen in Equation 22.

$$\boldsymbol{x}_0 = \boldsymbol{x}_{SL_1} + \epsilon\hat{\zeta}_{1,SL_1} \tag{22a}$$

$$\boldsymbol{x}_0 = \boldsymbol{x}_{SL_2} - \epsilon\hat{\zeta}_{1,SL_2} \tag{22b}$$

where $\hat{\zeta}_{1,SL_1}$ and $\hat{\zeta}_{1,SL_2}$ are the unit eigenvectors associated with the negative real eigenvalues for SL_1 and SL_2, respectively.

Further analysis is performed on these two initial conditions. The initial generation algorithm is run for 30 varying seeds, with the standard in-built *MATLAB*$^{(R)}$ Random Number Generator (RNG), elitism of 1%, and 1000 MC runs per leg for each of the two initial conditions in Equation 22. The definition of these parameters is provided in subsection V.D. The results are shown in Table 3, which shows a considerably higher number of fly-bys for the positive perturbation from SL_1 compared to the negative perturbation from SL_2. Therefore it is decided to use the positive perturbation from SL_1 to generate the initial trajectory.

	SL_1	SL_2
Minimum	8	5
Maximum	13	10
Mean	10.83	7.25

Table 3 Number of asteroid fly-bys for differing starting conditions.

D. Sequence Generation Algorithm Tuning

Testing and tuning of the sequence generation code is performed, using the findings from the search space analysis for the first leg. Little analysis can be performed on subsequent legs of the trajectory, as there is a wide range of possible ending conditions of the first leg. The parameters related to the sequence generation algorithm that can be varied are as follows.

1) The random number generator (RNG): Random values for the decision variables in $\boldsymbol{h}_i$ in Equation 20 are generated at each leg, and the method of generating random numbers to select these decision variables can be varied.

2) The proportion of *elitism*: Each subsequent leg after the first is started from the end point of a previous leg, selected from a subset of the best-performing trajectories (i.e. closest fly-bys in the shortest time), and the proportion of previous legs to carry forward for use as the starting location of the next leg can be varied.
3) The number of random samples to generate at each leg: A Monte Carlo (MC) search is performed at each leg to identify the best performing combinations of solar sail settings, and the number of MC runs to perform can be adjusted.

The parameters are sequentially tested and the findings for each parameter are used for testing of subsequent parameters.

1. Random Number Generator

Two RNGs are compared to determine their performance within the sequence generation algorithm. The in-built RNG in *MATLAB*$^{\text{(R)}}$, which is called through the *rand.m* function, returns a randomly selected distribution on the open interval $(0, 1)$. A quasi-random Sobol sequence is called through the *sobolset.m* function to also generate a uniform distribution of points in the open interval $(0, 1)$. The Sobol sequence selects values from a highly uniform distribution of points within a hyper-sphere [48].

The in-built RNG in *MATLAB*$^{\text{(R)}}$ is implemented with a fixed seed to allow for reproducibility. Similarly, to increase the possible values that the variables can take, and to allow reproducibility, the Sobol sequence is sampled at a random point along its distribution depending on the seed value.

The performance of the developed algorithm with the in-built RNG and the quasi-random Sobol sequence are compared. As the parameters for the in-built RNG are the same as those in the previous section, the findings from Table 3 are re-used. The sequence generation algorithm is run for the Sobol sequence sampled randomly with 30 different seed values, 1000 MC samples per leg, and elitism of 1%. The starting location is fixed at SL_1 based on the previous results.

	rand.m	Sobol
Minimum	8	9
Maximum	13	13
Mean	10.83	11.50

Table 4 Number of asteroid fly-bys for differing RNGs.

It can be seen that there is a slight improvement in the results when the Sobol sequence is used over the in-built RNG in *MATLAB*$^{\text{(R)}}$. The minimum number of fly-bys found and the mean both increase, but the maximum is the same for both the Sobol and the *rand.m* function. Due to the better performance on average, the Sobol method is selected as the chosen random number generator.

2. Elitism

The proportion of current trajectories to use when generating the next leg of the trajectory can have a significant effect on the performance of the algorithm. This proportion of current trajectories carried forward is referred to as elitism. At each step of the algorithm, the trajectories are ranked based on the most encounters within the shortest flight time. The elitism proportion of these trajectories are brought forward to be used as starting conditions for the next leg of the trajectory. In the case of the elitism resulting in a non-whole number, the number of legs carried forward is rounded up to the nearest integer.

Testing of this elitism proportion is carried out to determine the best performing proportion of current legs to carry forward at each stage of the trajectory. Similar to the previous parameters tested, a range of seed numbers for each setting is implemented. Elitism values of 1%, 0.5%, and 0.1% are tested with the Sobol sequence and 1000 MC runs per leg, for 30 different seed values. The results of this testing can be seen in Table 5. It can be seen that an elitism value of 0.5% provides the best results for both the minimum, maximum, and mean. This value is thus chosen as the parameter value for the final sequence generation.

	1%	0.5%	0.1%
Minimum	9	10	8
Maximum	13	16	15
Mean	11.50	13.90	13.16

Table 5 Number of asteroid fly-bys for differing elitism values.

3. Monte Carlo Runs per Leg

Finally, the number of MC runs to perform at each leg is tested. Increasing this value increases the number of samples for cone and clock angle that can be selected which improves the performance of the algorithm, but it also decreases the speed at which full trajectories can be generated. A compromise thus needs to be found that balances the performance of the algorithm with the run time.

MC runs per leg values of 1000, 2500, and 5000 are tested for each leg with 20 different seed values, with the Sobol sequence generator and elitism of 0.5%. The run-time is greatly increased with an increase in the number of MC runs per leg, so the number of various seed values to test is decreased from 30 to 20. Parallel processing is employed within *MATLAB*$^{\text{(R)}}$ to reduce the total run time. As can be seen in Table 6, increasing the number of random trajectories generated at each leg from 1000 to 2500 led to an increase in the average and maximum number of encounters over the ten year period. However, increasing beyond 2500 per leg resulted in considerably longer computation time, with no improvement on the maximum number of encounters, and only a slight increase in the average number of encounters. Thus, a value of 2500 MC runs is selected to be performed at each leg of the sequence generation algorithm.

	1000	2500	5000
Minimum	10	12	13
Maximum	16	17	17
Mean	13.90	15.16	15.33
Average Run Time [min]	21	50	126

Table 6 Number of asteroid fly-bys and average run time for differing numbers of MC runs performed at each leg.

E. Finalised Initial Trajectory

The chosen parameter values are implemented and the algorithm is run for 30 different seeds values. The final settings and parameter values and ranges can be seen in Table 7.

Parameter	Selection or range
Initial condition, $\boldsymbol{x}_{0,1}$	SL_1, positive perturbation as in Equation 22a
Initial time, $t_{0,1}$	$\in$ [1 Jan 2025, 31 Dec 2026]
Cone angle, α [rad]	$\in \left[-\frac{\pi}{2},\ \frac{\pi}{2}\right]$
Clock angle, δ [rad]	$\in [0,\ \pi]$
RNG	Sobol sequence
Elitism	0.5 %
MC runs per leg	2500
Seed values	$\in$ [5368111, 5368141]

Table 7 Sequence generation chosen parameter values.

Due to the complex nature of the problem, and the large number of possible sequences of asteroids, each run with a different seed value produces a different result. The trajectory with the most encounters from each of the developed trajectories with varying seeds is selected. This trajectory has 18 total fly-bys of 15 unique asteroids within the nominal mission lifetime of ten years, with the final fly-by occurring after 9.02 years. The trajectory viewed on the $x - y$ and $x - z$ planes can be seen in Figure 8. The full control profile for the entire mission can also be seen here. This full trajectory departs the SL_1 point on the 7th of July, 2026. The fixed cone and clock angles, α and δ, as well as the fly-by distance of each asteroid and transfer time between targets can be seen in Table 8.

VI. Optimisation

This section discusses the optimisation of the first fly-by of the initial trajectory generated in Section V. The optimisation of the first fly-by is provided as a proof of concept for the rest of the trajectory. Firstly, the optimal control problem which is to be solved is introduced, and some tuning of the optimisation software is discussed. A description of the initial guess used as input to the optimisation software is then provided. Finally, the optimised solution is presented and discussed.

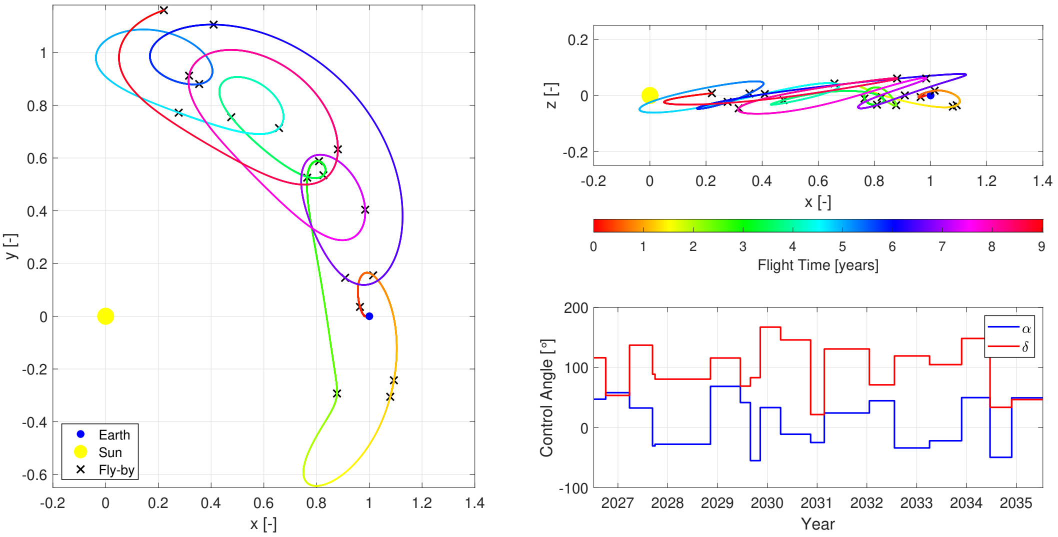

Fig. 8 **Full solar sailing initial trajectory viewed in the $x-y$ and $x-z$ planes and full control profile.**

A. Optimal Control Problem

During the initial trajectory design phase, an encounter was taken as a fly-by within 5×10^5 km of an asteroid. In this section, however, the relative fly-by distance and velocity between the solar sailing spacecraft and the asteroid is minimised. This optimisation is performed for one fly-by of the initial trajectory as a proof of concept that each fly-by can be optimised individually. The optimisation of the first fly-by is performed by optimising the first two legs of the trajectory - the leg from SL$_1$ to the first target asteroid, and the leg from the first target to the second target, with the objective of re-joining the initial fixed-angle developed trajectory at the fly-by of the second asteroid. This ensures that the optimisation of the first fly-by does not hinder any further elements of the trajectory.

1. Leg 1

The objective function, J_1, for the first leg of the trajectory is

$$J_1 = \Delta r^{(1)} + w \Delta v^{(1)} \tag{23}$$

where $\Delta r^{(1)} = |\boldsymbol{r}_f^{(1)} - \boldsymbol{r}_{ast,f}^{(1)}|$ and $\Delta v^{(1)} = |\boldsymbol{v}_f^{(1)} - \boldsymbol{v}_{ast,f}^{(1)}|$ are the relative position and velocity respectively between the spacecraft and the target asteroid at the final time of the first leg, $t_f^{(1)}$, $\boldsymbol{r}_f^{(1)} = \boldsymbol{r}(t_f^{(1)})$ and $\boldsymbol{v}_f^{(1)} = \boldsymbol{v}(t_f^{(1)})$ are the final position and velocity vectors of the spacecraft, $\boldsymbol{r}_{ast,f}^{(1)} = \boldsymbol{r}_{ast}(t_f^{(1)})$ and $\boldsymbol{v}_{ast,f}^{(1)} = \boldsymbol{v}_{ast}(t_f^{(1)})$ are the final position and velocity vectors of the target asteroid, and w is a weight for the relative velocity.

The goal of the optimisation is to find the states, $\boldsymbol{x}^{(1)}(t)$, and controls, $\boldsymbol{u}^{(1)}(t)$, that minimise Eq. 23 while satisfying the dynamics in Eq. 1 as well as a set of boundary constraints. The state vector, $\boldsymbol{x}^{(1)}(t)$, refers to the position and

Leg	**Cone Angle**, α [°]	**Clock Angle**, δ [°]	**Fly-by Distance** [km]	**Flight Time** [days]	**Fly-by Date**	**Target Asteroid**
1	47.31	116.16	307702.40	87.71	03-Oct-26	2020 GE1
2	58.16	53.56	426592.93	174.66	26-Mar-27	2021 GN1
3	32.64	137.18	434969.06	168.71	11-Sep-27	2005 QQ87
4	-30.51	88.83	496219.28	18.61	30-Sep-27	2020 TH6
5	-27.63	80.65	419607.65	406.48	09-Nov-28	2019 SB6
6	68.63	115.82	450347.46	219.39	17-Jun-29	2021 BA
7	41.69	69.08	447909.54	73.53	29-Aug-29	2015 SO2
8	-54.94	83.15	487291.59	72.27	09-Nov-29	2015 YA
9	33.35	167.23	443346.64	149.27	08-Apr-30	2021 XS4
10	-10.97	145.89	470736.86	220.13	14-Nov-30	2018 PN22
11	-24.78	21.75	397484.29	100.55	22-Feb-31	2019 VL5
12	24.32	130.85	324486.45	330.33	19-Jan-32	2015 SO2
13	44.68	71.15	450440.39	183.99	21-Jul-32	2019 YB4
14	-33.84	119.24	413020.53	257.54	04-Apr-33	2020 TH6
15	-21.91	104.83	359357.28	235.23	25-Nov-33	2018 XW2
16	49.91	148.34	265905.52	208.45	22-Jun-34	2016 CO246
17	-49.46	33.77	499834.17	158.75	28-Nov-34	2017 YQ5
18	49.52	46.68	258702.24	228.70	14-Jul-35	2019 YB4

Table 8 Trajectory settings for each leg.

velocity vectors of the spacecraft within the CR3BP:

$$\boldsymbol{x}^{(1)}(t) = [\boldsymbol{r} \;\; \dot{\boldsymbol{r}}]^T = [x(t) \;\; y(t) \;\; z(t) \;\; \dot{x}(t) \;\; \dot{y}(t) \;\; \dot{z}(t)]^T \tag{24}$$

The initial state of the first leg needs to match the perturbed state at the SL$_1$ point as in Equation 22a, and the objective is for the final state to coincide with the asteroid's state vector at time t_f, i.e.

$$\boldsymbol{x}(t_0^{(1)}) = \boldsymbol{x}_0^{(1)} = \boldsymbol{x}_{SL_1} + \epsilon\hat{\boldsymbol{\zeta}}_{1,SL_1} \tag{25a}$$

$$\boldsymbol{x}(t_f^{(1)}) = \boldsymbol{x}_f^{(1)} = \boldsymbol{x}_{ast,f} \tag{25b}$$

where $\boldsymbol{x}_{ast,f}$ is the state vector of the asteroid at time t_f.

Suitable bounds are placed on the state vector as follows

$$[0.8 \;\; -0.1 \;\; -0.05 \;\; -0.1 \;\; -0.1 \;\; -0.1]^T \le \boldsymbol{x}^{(1)}(t) \le [1.0 \;\; 0.3 \;\; 0.05 \;\; 0.1 \;\; 0.15 \;\; 0.1]^T \tag{26}$$

The controls are defined as the cone and clock angles of the solar sail:

$$\boldsymbol{u}^{(1)}(t) = [\alpha \;\; \delta]^T \tag{27}$$

with the following imposed bounds:

$$\left[-\frac{\pi}{2} \;\; 0\right]^T \leq \boldsymbol{u}^{(1)}(t) \leq \left[\frac{\pi}{2} \;\; \pi\right]^T \tag{28}$$

Bounds on the initial and final time are also specified to ensure the trajectory targets the first asteroid near the the initially determined fly-by date (see the first row in Table 8), which will also ensure that the second target asteroid can be reached after the first fly-by. Bounds of ±5 days are placed on the initial time. The departure time is time-independent and can theoretically take any value, as long as the trajectory returns to the initial trajectory at the fly-by of the second asteroid.

2. Leg 2

The second leg of the trajectory is optimised after the first, with the objective of re-joining the initial fixed-angle developed trajectory at the fly-by of the second asteroid. The objective function for the second leg of the trajectory is

$$J_2 = \Delta r^{(2)} + w\Delta v^{(2)} \tag{29}$$

where $\Delta r^{(2)}$ and $\Delta v^{(2)}$ are the relative distance and velocity between the spacecraft and the second target asteroid at the end of the second leg, and w is the same weight as in Equation 23.

The initial time for the second leg, $t_0^{(2)}$, is set as the final time of the first leg, i.e. $t_0^{(2)} = t_f^{(1)}$, while the final time of the second leg, $t_f^{(2)}$, is set to the fly-by time of the second asteroid in the initially developed trajectory, i.e. 26th March 2027 (see Table 8). The initial state of the second leg, $\boldsymbol{x}(t_0^{(2)}) = \boldsymbol{x}_0^{(2)}$, is set to the final state of the optimised first leg, i.e. $\boldsymbol{x}_0^{(2)} = \boldsymbol{x}_f^{(1)}$, and the objective of the second leg is to coincide with the state at fly-by of the second asteroid in the initially developed trajectory.

The bounds imposed on the state and control vectors for the second leg are the same as for the first leg, as in Equation 26 and Equation 28.

3. PSOPT

The optimal control problems defined above is solved using PSOPT, an open-source direct pseudospectral method implemented in C++ [47]. PSOPT has been used for the optimisation of solar sailing missions in previous studies [8, 10, 28]. PSOPT directly discretizes the original optimal control problem over the continuous time interval into a finite number of collocation points (nodes). Either Legendre or Chebyshev polynomials can be used to approximate the state profile at the nodes, and in this case only Legendre polynomials are used. PSOPT formulates an NLP problem, which is then interfaced to the solver IPOPT (Interior Point OPTimiser), and then numerically solved [49]. PSOPT ensures that the dynamics are satisfied and the constraints are met only at the nodes of the solution. The PSOPT solution can be re-integrated to verify the validity of the solution and determine if the constraints and dynamics are satisfied along the entire solution.

4. *Optimiser Tuning*

A grid search is performed to analyse combinations of convergence tolerances and initial mesh sizes in PSOPT and IPOPT. The results of this grid search can be seen in Figure 9. Due to the complex nature of this problem, PSOPT fails to find an optimal solution for many combinations of mesh size and tolerance, as can be seen in Figure 9. An initial mesh size of 50 nodes and a convergence tolerance of 5×10^{-4} is selected from Figure 9, and a maximum number of iterations of 1000 is enforced.

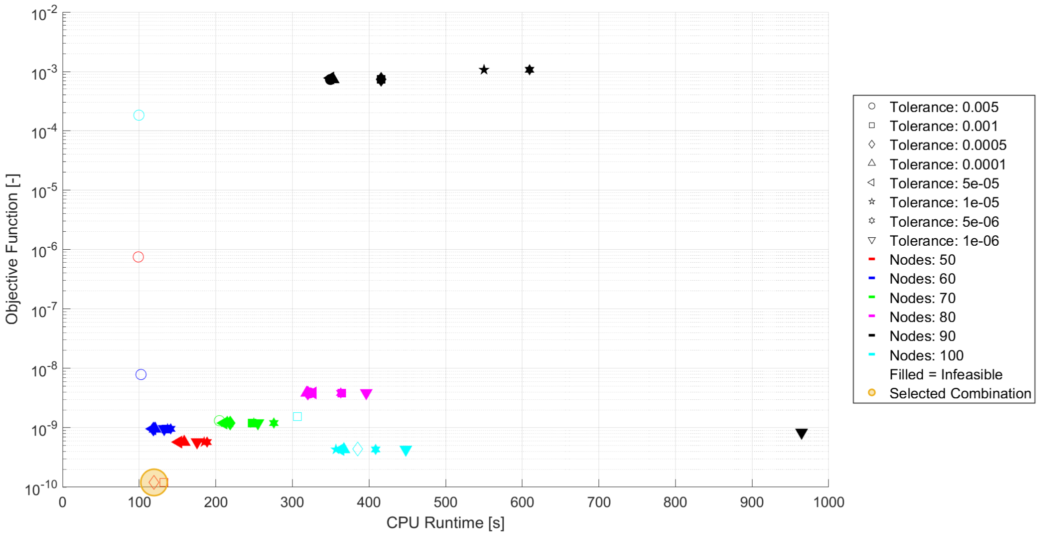

Fig. 9 Grid search results for PSOPT initial mesh size and tolerance.

Testing is then performed on the bounds for the final time of the first leg, $t_f^{(1)}$, to determine a suitable constraint value. Similarly, values for the weight in the objective function, w, are tested to determine a suitable value. The results from the testing of both of these parameters can be seen in Figure 10, where the left plot contains the final time bounds testing, and the right plot contains weight testing results. It is found that bounds of ±4.5 days on the final time provides converged results with the lowest objective function value. This is therefore chosen as the parameter value for the final optimisation. The value for the weight in the objective function, w, is chosen as 10^{-3}, as this gives a considerably lower relative fly-by distance, and a reduction in relative fly-by velocity. These parameters are combined and implemented in PSOPT to find the optimised solution.

5. *Initial Guess*

PSOPT requires an initial guess as input in order to generate an optimal solution. This input contains the time, states, and control vectors of the initial guess. In the problem investigated in this paper, the initial guess is taken as

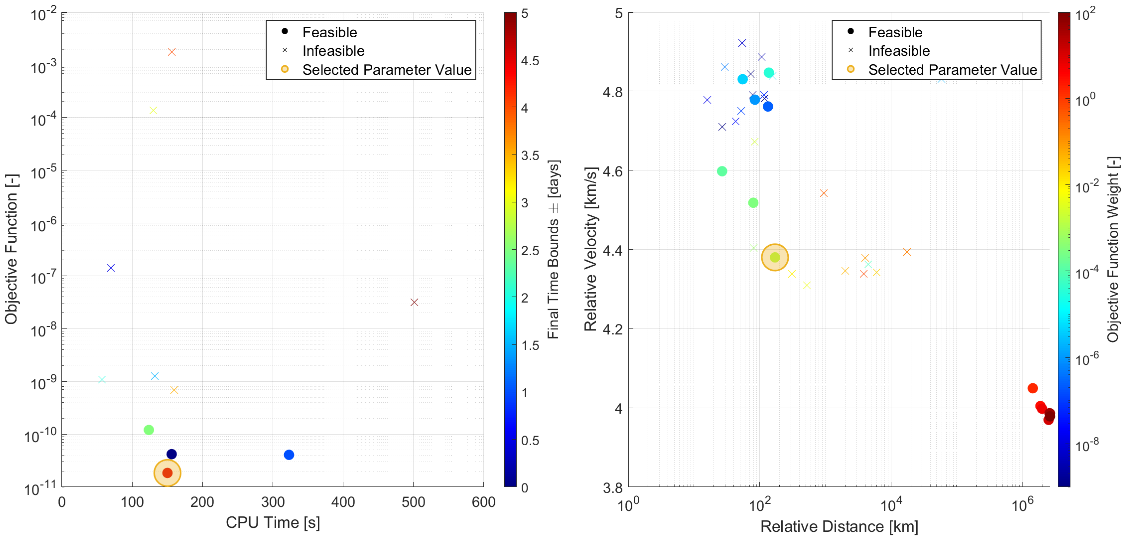

Fig. 10 Parameter testing on the bounds of the final time of the first leg, and objective function weight, w.

the fixed-angle trajectory for each leg of the initial trajectory design. The trajectory and control profile can be seen in Figure 8.

B. Results

The described optimal control problem is implemented in PSOPT and solved. Mesh refinement is performed in PSOPT by interpolating a previous solution onto a new mesh which has a larger number of nodes. The initial number of nodes, 50, is refined to 100 and then 150 nodes consecutively for both the first and second legs. The first and second legs are solved separately, with the findings from the optimisation of the first leg used as input and constraints for the second leg. The resulting relative fly-by distance and velocity for both legs, as well as the departure and fly-by dates of the initial and optimised solutions can be seen in Table 9. It can be seen that there is a significant reduction in the fly-by distance, as well as a slight decrease in the relative fly-by velocity of the first target. The flight time is also slightly longer, departing two days earlier than the initial guess and arriving a day later. It can also be seen that the fly-by conditions of the second leg coincide exactly for both the initial guess and the PSOPT solution, validating the return

	Leg 1		**Leg 2**	
	Initial Guess	**PSOPT Solution**	**Initial Guess**	**PSOPT Solution**
Relative Fly-by Distance [km]	307, 702	158.73	426, 593	426, 593
Relative Fly-by Velocity [km/s]	4.7923	4.3282	3.4083	3.4083
Departure Date	7th July 2026	5th July 2026	3rd October 2026	6th October 2026
Fly-by Date	3rd October 2026	6th October 2026	26th March 2027	26th March 2027

Table 9 Initial guess and PSOPT solution results.

of the optimised trajectory to the initial trajectory. The trajectory and control profile found by PSOPT can be seen in Figure 11. The light blue and pink lines in the trajectory plots are the first and second leg solutions found by PSOPT respectively. The light blue line in the control angle plot in the bottom right is the solution cone angle for the entire two legs, α_{SOL}, while the pink line is the solution clock angle, δ_{SOL}. It can be seen in both Table 9 and Figure 11 that the spacecraft travels much closer to the asteroid than with the initial guess. This closer fly-by is obtained by a much more complex control profile than the fixed-angle control profile from the sequence generation algorithm.

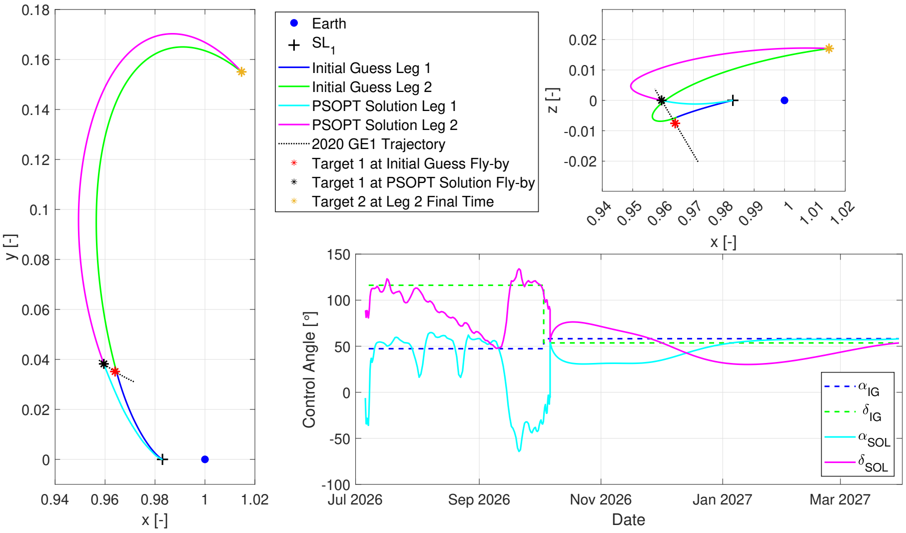

Fig. 11 Initial guess and PSOPT solution trajectories and control profiles.

C. Solution Re-integration

Re-integration can be performed to verify the validity of the PSOPT solution and determine if the constraints and dynamics are satisfied along the entire solution. This re-integration is performed by integrating the state of the spacecraft from the initial to the final solution times, from the initial condition of the PSOPT solution. The controls, $\boldsymbol{u}(t)$ are interpolated from the PSOPT control solution at each integration time step using the *MATLAB*$^{(R)}$ built-in linear interpolation method, *interp1.m*. The difference between the final state of the PSOPT solution and the re-integrated solution indicates the validity of the PSOPT implementation. The re-integrated solution is presented in Figure 12, where it can be seen the re-integration matches the PSOPT solution very closely. The position and velocity errors at the end of the re-integration are 41.6721×10^{-6} and 32.0351×10^{-6} in dimensionless units, respectively. These values are below the selected PSOPT tolerance of 5×10^{-4}, thus verifying the solution.

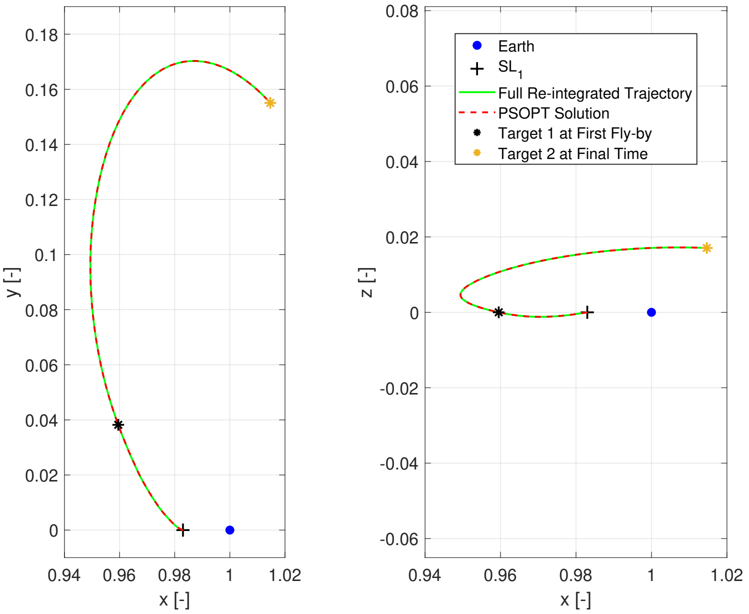

Fig. 12 Original PSOPT output and re-integrated solution.

VII. Conclusion

It has been shown in this paper that solar sailing is a suitable means of propulsion to rendezvous with multiple co-orbital NEAs during one mission, within a set of assumed mission constraints. A trajectory to multiple co-orbital NEAs within a nominal mission lifetime is developed, and the first two legs of this trajectory are optimised for relative fly-by distance and velocity between the spacecraft and the first target asteroid. Firstly, an algorithm is developed for generating sequences of asteroids that can be visited using a solar sail with a fixed-angle control law for each leg. This algorithm can produce solar sail trajectories that travel from asteroid to asteroid using fixed cone and clock angles. This algorithm is tuned before producing the final sequence of asteroids to visit for this research. Finally, the first fly-by of this trajectory is optimised for fly-by distance and velocity, as a proof of concept that each leg can be optimised. This optimised first fly-by does not hinder the remainder of the trajectory, as the state at the second fly-by of the optimised solution and of the initial trajectory are the same.

It has been shown that the developed sequence generation algorithm is capable of developing trajectories with many fly-bys within the nominal mission lifetime. The finalised fixed-angle control law trajectory in this research contains 18 fly-bys of 15 unique asteroids, which is roughly a fly-by every six months of flight. However, analysis of the algorithm has shown that varying the seed number varies the number of fly-bys largely, so it is possible that running the algorithm with a larger number of seed values would result in even more fly-bys. The bounds on the initial time could also be increased to account for a wider range of departure dates, which would lead to different sequences of targets to visit and possibly a larger number of fly-bys for the same mission time. A mission trajectory with 18 fly-bys would significantly reduce the cost of missions to asteroids, as there is only one development and launch cost for the entire mission rather than for each target. It can be concluded that this developed algorithm is an effective method of generating sequences of asteroids to visit with fixed-angle solar sail transfers between targets.

It has also been shown that the relative fly-by distance and velocity between the spacecraft and the target can be significantly reduced using an optimisation stage. The relative distance of the first fly-by was reduced from $307,702$ km to 158.73 km, which is a 99.95% reduction, while the relative velocity was reduced from 4.7923 km/s to 4.3282 km/s, which is a reduction of 9.68%. This shows that a direct pseudospectral method, implemented through PSOPT, is a suitable method of optimising the initial trajectory.

The developed sequence generation algorithm focuses on finding trajectories that are within a minimum fly-by distance of a target asteroid, and neglects the relative velocity of this fly-by. This can lead to fly-bys with quite a large relative velocity, which can be sub-optimal conditions for analysis to take part during a fly-by, and also reduces the time in vicinity of the target. The sequence generation algorithm could be adjusted to include a weighted relative velocity, which would allow for trajectories that are more suitable for analysis of a target. This would likely reduce the number of fly-bys that occur within the mission lifetime.

The proposed solar sailing trajectory developed in this paper would be an effective method of visiting and analysing multiple asteroids within the same mission. This mission could help further investigate the target asteroids, which would benefit research into the early solar system, help to classify the asteroids for planetary defence, or analyse the asteroids for future space mining.

References

[1] O. Mori, Y. Shirasawa, Y. Mimasu, Y. Tsuda, H. Sawada, T. Saiki, T. Yamamoto, K. Yonekura, H. Hoshino, J. Kawaguchi, and R. Funase. Overview of IKAROS Mission. In M. Macdonald, editor, *Advances in Solar Sailing*, pages 25–43. Springer Berlin Heidelberg, Berlin, Heidelberg, 2014. ISBN 978-3-642-34907-2. doi: 10.1007/978-3-642-34907-2{_}3.

[2] Y. Tsuda, O. Mori, R. Funase, H. Sawada, T. Yamamoto, T. Saiki, T. Endo, K. Yonekura, H. Hoshino, and J. Kawaguchi. Achievement of IKAROS-Japanese deep space solar sail demonstration mission. In *Acta Astronautica*, volume 82, pages 183–188, 2013. doi: 10.1016/j.actaastro.2012.03.032.

[3] G. Vulpetti, L. Johnson, and G. L. Matloff. The NanoSAIL-D2 NASA Mission. In *Solar Sails : A Novel Approach to Interplanetary Travel*, Springer Praxis Books : Space Exploration TA - TT -, pages 173–178. New York, NY : Springer New York : Springer, 2015. ISBN 978-1-4939-0940-7. doi: 10.1007/978-1-4939-0941-4{_}16LK-https://tudelft.on.worldcat.org/oclc/5694009621.

[4] D. A. Spencer, B. Betts, J. M. Bellardo, A. Diaz, B. Plante, and J. R. Mansell. The LightSail 2 solar sailing technology demonstration. *Advances in Space Research*, 67(9):2878–2889, 2021. ISSN 18791948. doi: 10.1016/j.asr.2020.06.029.

[5] B. Betts, D. A. Spencer, J. M. Bellardo, B. Nye, A. Diaz, B. Plante, J. Mansell, M. A. Fernandez, C. T. Gillespie, and D. Garber. LightSail 2: Controlled solar sail propulsion using a CubeSat. In *Proceedings of the International Astronautical Congress, IAC*, volume 2019-Octob, page 7, 2019.

[6] L. McNutt, L. Johnson, D. Clardy, J. Castillo-Rogez, A. Frick, and L. Jones. Near-Earth Asteroid Scout. In *AIAA SPACE 2014 Conference and Exposition*, page 9, 2014. ISBN 9781624102578. doi: 10.2514/6.2014-4435.

[7] NASA. Advanced Composite Solar Sail System. *NASAfacts*, pages 6–7, 2020.

[8] A. Farrés, J. Heiligers, and N. Miguel. Road map to L4/L5 with a solar sail. *Aerospace Science and Technology*, 95:105458, 2019. ISSN 12709638. doi: 10.1016/j.ast.2019.105458.

[9] A. Farrés and A. Jorba. Station Keeping Strategies for a Solar Sail in the Solar System. In B. Bonnard and M. Chyba, editors, *Recent Advances in Celestial and Space Mechanics*, pages 83–115. Springer, 2016. ISBN 9781618398055. doi: 10.1007/978-3-319-27464-5.

[10] J. Heiligers, B. Diedrich, B. Derbes, and C. R. Mcinnes. Sunjammer: Preliminary end-to-end-mission design. *AIAA/AAS Astrodynamics Specialist Conference 2014*, 1(June 2016), 2014. doi: 10.2514/6.2014-4127.

[11] A. Farrés and A. Jorba. Solar sailing with invariant manifolds in the earth-sun system. *Proceedings of the International Astronautical Congress, IAC*, 7(October 2015):5323–5333, 2015. ISSN 00741795.

[12] R. Sood and K. Howell. Solar Sail Transfers and Trajectory Design to Sun-Earth L 4, L 5: Solar Observations and Potential Earth Trojan Exploration. *Journal of the Astronautical Sciences*, 66(3):247–281, 2019. ISSN 21950571. doi: 10.1007/s40295-018-00141-4.

[13] J. Heiligers and C. R. McInnes. Agile solar sailing in three-body problem: Motion between artificial equilibrium points. *Proceedings of the International Astronautical Congress, IAC*, 7:5439–5451, 2013. ISSN 00741795.

[14] M. J. Drake, K. Righter, and E. Scott. Compositional Relationships Between Meteorites and Terrestrial Planets. *Meteorites and the Early Solar System II*, pages 803–828, 2003.

[15] D. Sivolella. *Space Mining and Manufacturing: Off-World Resources and Revolutionary Engineering Techniques*. Springer, 2019. ISBN 9783030308803.

[16] M. Yoshikawa, J. Kawaguchi, A. Fujiwara, and A. Tsuchiyama. The Hayabusa mission. In *Sample Return Missions*, pages 123–146. Elsevier Inc., 2021. doi: 10.1016/b978-0-12-818330-4.00006-9.

[17] Y. Tsuda, T. Saiki, F. Terui, S. Nakazawa, M. Yoshikawa, and S. i. Watanabe. Hayabusa2 mission status: Landing, roving and cratering on asteroid Ryugu. *Acta Astronautica*, 171(January):42–54, 2020. ISSN 00945765. doi: 10.1016/j.actaastro.2020.02.035.

[18] D. S. Lauretta, H. L. Enos, A. T. Polit, H. L. Roper, and C. W. V. Wolner. OSIRIS-REx at Bennu: Overcoming challenges to collect a sample of the early Solar System. *Sample Return Missions*, 1:163–194, 2021. doi: 10.1016/c2018-0-03374-5.

[19] L. Prockter, S. Murchie, A. Cheng, S. Krimigis, R. Farquhar, A. Santo, and J. Trombka. The NEAR Shoemaker mission to asteroid 433 Eros. *Acta Astronautica*, 51(1-9):491–500, 2002. ISSN 00945765. doi: 10.1016/S0094-5765(02)00098-X.

[20] NASA. Overview | Dawn NASA Solar System Exploration, 2021, `https://solarsystem.nasa.gov/missions/dawn/overview/` (Accessed: 2021-09-24).

[21] NASA/JPL. Deep Space 1, 2021, `https://www.jpl.nasa.gov/missions/deep-space-1-ds1` (Accessed: 2021-09-30).

[22] K. Altwegg, P. Martin, and M. Taylor. Rosetta mission. *Access Science*, 2016. doi: 10.1036/1097-8542.YB150700.

[23] C. B. Olkin, H. F. Levison, M. Vincent, K. S. Noll, J. Andrews, S. Gray, P. Good, S. Marchi, P. Christensen, D. Reuter, H. Weaver, M. Pätzold, J. F. Bell, V. E. Hamilton, N. D. Russo, A. Simon, M. Beasley, W. Grundy, C. Howett, J. Spencer, M. Ravine, and M. Caplinger. Lucy mission to the Trojan asteroids: Instrumentation and encounter concept of operations. *Planetary Science Journal*, 2(5), 2021. ISSN 26323338. doi: 10.3847/PSJ/abf83f.

[24] C. de la Fuente Marcos and R. de la Fuente Marcos. Asteroid 2017 FZ2 et al.: Signs of recent mass-shedding from YORP? *Monthly Notices of the Royal Astronomical Society*, 473(3):3434–3453, 2018. ISSN 13652966. doi: 10.1093/mnras/stx2540.

[25] C. de la Fuente Marcos and R. de la Fuente Marcos. A trio of horseshoes: past, present and future dynamical evolution of Earth co-orbital asteroids 2015 XX169, 2015 YA and 2015 YQ1. *Astrophysics and Space Science*, 361(4):1–15, 2016. ISSN 1572946X. doi: 10.1007/s10509-016-2711-6.

[26] C. de La Fuente Marcos and R. de La Fuente Marcos. From horseshoe to quasi-satellite and back again: the curious dynamics of Earth co-orbital asteroid 2015 SO2. *Astrophysics and Space Science*, 361(1):1–10, 2016. ISSN 1572946X. doi: 10.1007/s10509-015-2597-8.

[27] C. de la Fuente Marcos and R. de la Fuente Marcos. A resonant family of dynamically cold small bodies in the near-earth asteroid belt. *Monthly Notices of the Royal Astronomical Society: Letters*, 434(1):1–5, 2013. ISSN 17453925. doi: 10.1093/mnrasl/slt062.

[28] J. Heiligers, J. M. Fernandez, O. R. Stohlman, and W. K. Wilkie. Trajectory design for a solar-sail mission to asteroid 2016 HO3. *Astrodynamics*, 3(3):231–246, 2019. ISSN 25220098. doi: 10.1007/s42064-019-0061-1.

[29] T. Hamasaki and J. Kawaguchi. Solar sail trajectory design for exploration of asteroids from/to space port around L2 point. In *Advances in the Astronautical Sciences*, volume 150, pages 3399–3417, 2014. ISBN 9780877036050.

[30] A. Peloni, M. Ceriotti, and B. Dachwald. Solar-sail trajectory design for a multiple near-earth-asteroid rendezvous mission. *Journal of Guidance, Control, and Dynamics*, 39(12):2712–2724, 2016. ISSN 15333884. doi: 10.2514/1.G000470.

[31] A. Peloni, B. Dachwald, and M. Ceriotti. Multiple near-earth asteroid rendezvous mission: Solar-sailing options. *Advances in Space Research*, 62(8):2084–2098, 2018. ISSN 18791948. doi: 10.1016/j.asr.2017.10.017.

[32] K. F. Wakker. *Fundamentals of Astrodynamics*. Institutional Repository, Delft University of Technology Library, 2015. ISBN 9789461864192. doi: 10.1007/978-3-319-09444-1{_}1.

[33] J. B. Pezent, R. Sood, and A. Heaton. Configuration space and stability analysis of solar sail near-vertical earth-trailing orbits. *Advances in Space Research*, 67(9):2981–2994, 2021. ISSN 18791948. doi: 10.1016/j.asr.2020.10.011.

[34] Z. E. Musielak and B. Quarles. The three-body problem. *Reports on Progress in Physics*, 77(6), 2014. ISSN 00344885. doi: 10.1088/0034-4885/77/6/065901.

[35] C. R. McInnes. *Solar Sailing: Technology, Dynamics and Mission Applications*. Springer-Verlag Berlin Heidelberg, 1 edition, 2004. ISBN 978-3-540-21062-7.

[36] T. Pino, C. Circi, and G. Vulpetti. Wrinkling analysis for small solar-photon sails: An experimental and analytic approach for trajectory design. *Advances in Space Research*, 63(11):3675–3690, 2019. ISSN 18791948. doi: 10.1016/j.asr.2019.02.016.

[37] J. M. Fernandez, G. K. Rose, O. R. Stohlman, C. J. Younger, G. D. Dean, J. E. Warren, J. H. Kang, R. G. Bryant, and W. K. Wilkie. An advanced composites-based solar sail system for interplanetary small satellite missions. *AIAA Spacecraft Structures Conference, 2018*, 2018. doi: 10.2514/6.2018-1437.

[38] A. F. Mora and J. Heiligers. Solar-sail quasi-periodic orbits in the sunearth system. *Journal of Guidance, Control, and Dynamics*, 43(9):1740–1749, 2020. ISSN 15333884. doi: 10.2514/1.G005021.

[39] W. K. Wilkie, J. M. Fernandez, O. R. Stohlman, N. R. Schneider, G. D. Dean, J. H. Kang, J. E. Warren, S. M. Cook, P. L. Brown, T. C. Denkins, S. D. Horner, E. D. Tapio, M. Straubel, M. Richter, and J. Heiligers. An overview of the NASA advanced composite solar sail (ACS3) technology demonstration project. *AIAA Scitech 2021 Forum*, pages 1–23, 2021.

[40] F. Topputo. Fast numerical approximation of invariant manifolds in the circular restricted three-body problem. *Communications in Nonlinear Science and Numerical Simulation*, 32:89–98, 2016. ISSN 10075704. doi: 10.1016/j.cnsns.2015.08.004.

[41] F. Topputo, M. Vasile, and F. Bernelli-Zazzera. Low energy interplanetary transfers exploiting invariant manifolds of the restricted three-body problem. *Journal of the Astronautical Sciences*, 53(4):353–372, 2005. ISSN 00219142. doi: 10.1007/bf03546358.

[42] C. de la Fuente Marcos and R. de la Fuente Marcos. Asteroid 2014 OL339: Yet another earth quasi-satellite. *Monthly Notices of the Royal Astronomical Society*, 445(3):2961–2970, 2014. ISSN 13652966. doi: 10.1093/mnras/stu1978.

[43] NASA. An Overview of Reference Frames and Coordinate Systems in the SPICE Context. Technical report, NASA, 2020.

[44] R. H. Battin. *An Introduction to the Mathematics and Methods of Astrodynamics, Revised Edition*. American Institute of Aeronautics and Astronautics Inc, AIAA, 1999. doi: 10.2514/4.861543.

[45] NASA, Princeton University, and Johns Hopkins Applied Physics Laboratory. IMAP Transfer Trajectory Initial State, 2019, `https://soma.larc.nasa.gov/stp/tdmo/pdf_files/2018-09-27_IMAP_Reference_LV_Transfer.pdf` (Accessed: 2022-05-23).

[46] ESA. PLATO Revealing habitable worlds around solar-like stars. *PLATO Definition Study Report*, 1(April), 2017.

[47] V. M. Becerra. Solving complex optimal control problems at no cost with PSOPT. In *Proceedings of the IEEE International Symposium on Computer-Aided Control System Design*, pages 1391–1396, 2010. ISBN 9781424453542. doi: 10.1109/CACSD.2010.5612676.

[48] I. M. Sobol. On the distribution of points in a cube and the approximate evaluation of integrals. *USSR Computational Mathematics and Mathematical Physics*, 7(4):86–112, 5 1967. ISSN 00415553. doi: 10.1016/0041-5553(67)90144-9.

[49] A. Wächter and L. T. Biegler. On the implementation of an interior-point filter line-search algorithm for large-scale nonlinear programming. *Mathematical Programming*, 106(1):25–57, 5 2006. ISSN 00255610. doi: 10.1007/s10107-004-0559-y.

Appendix

Table 10 Co-Orbital asteroids.

Asteroid Full Name	Semi-major axis, a $[AU]$	Eccentricity, e [-]	Inclination, i [°]	Orbital period, T $[days]$	Orbit Type
522684 (2016 JP)	0.9941	0.3834	11.3279	362.0361	QS
(2019 AE3)	0.9942	0.0997	14.8251	362.1006	TP
(2019 YB4)	0.9942	0.1925	0.54	362.1018	TP
(2019 EO)	0.9942	0.5325	9.3486	362.105	QS
(2007 FN3)	0.9946	0.2652	48.589	362.2931	HS
(2015 SO2)	0.9947	0.1088	9.1664	362.3324	HS
(2020 GE1)	0.9947	0.0855	7.7413	362.3773	TP
(2017 BG136)	0.9948	0.0525	27.6097	362.4148	TP
(2018 PN22)	0.9952	0.0441	4.4177	362.6242	HS
(2015 YA)	0.9954	0.2797	1.6186	362.7157	QS
(2009 WY104)	0.9955	0.2234	26.8007	362.7676	HS
(2009 HE60)	0.9955	0.2645	1.5832	362.7768	TP
(2019 HS2)	0.9956	0.2154	19.5494	362.8461	TP
(2021 BZ)	0.9956	0.3042	19.2866	362.8492	TP
(2009 PC)	0.9956	0.3427	7.0915	362.8615	QS
(2021 RE12)	0.9956	0.3658	21.7539	362.8697	QS
(2021 OT)	0.9958	0.3002	16.481	362.9471	QS
(2016 CO246)	0.9963	0.1261	6.2986	363.2172	TP
(2017 YQ5)	0.9972	0.1684	16.9824	363.7123	TP
(2018 XW2)	0.9974	0.3019	19.7377	363.8176	QS
(2017 SL16)	0.9975	0.1519	8.7934	363.8969	QS
3753 Cruithne (1986 TO)	0.9977	0.515	19.8068	364.0025	HS
(2021 XS4)	0.9977	0.189	14.6444	364.017	HS
(2021 EY1)	0.9977	0.455	6.0293	364.0231	HS
(2019 XQ1)	0.9979	0.2826	8.4997	364.0853	TP
85770 (1998 UP1)	0.998	0.3452	33.1796	364.188	HS
(2021 VH)	0.9983	0.1731	0.6128	364.3437	HS
(2017 XQ60)	0.9984	0.215	27.1923	364.3863	TP
(2021 GN1)	0.9988	0.1893	26.8994	364.5875	QS
(2014 OL339)	0.9989	0.4609	10.1852	364.6489	QS
(2010 TK7)	0.999	0.1905	20.8996	364.7049	TP
(2021 KO2)	0.999	0.4243	16.8215	364.7224	QS

(2021 UN7)	0.9991	0.3935	20.2835	364.7757	TP
(2016 CA138)	0.9995	0.0486	27.7271	364.9646	TP
(2019 VL5)	0.9999	0.2793	1.6589	365.2246	TP
(2020 PN1)	1.0002	0.1252	4.9479	365.3536	HS
(2020 CX1)	1.0006	0.1631	12.7414	365.5895	QS
(2020 XL5)	1.0007	0.3871	13.8474	365.6607	TP
(2005 QQ87)	1.001	0.3017	33.9712	365.7925	TP
469219 Kamo‘oalewa (2016 HO3)	1.0011	0.103	7.7889	365.8802	QS
255071 (2005 UH6)	1.0011	0.6324	2.6394	365.8847	HS
164207 (2004 GU9)	1.0013	0.136	13.6505	365.9584	QS
138852 (2000 WN10)	1.0013	0.2981	21.5108	365.9949	TP
(2020 PP1)	1.0014	0.0726	5.8991	366.032	QS
277810 (2006 FV35)	1.0015	0.3775	7.104	366.0519	QS
(2013 LX28)	1.0016	0.4519	49.9756	366.1499	QS
(2018 AN2)	1.002	0.1543	22.0747	366.3708	QS
441987 (2010 NY65)	1.0027	0.3704	11.5538	366.7242	TP
(2019 SB6)	1.003	0.266	7.1942	366.8864	QS
(2021 BA)	1.0031	0.2309	12.4696	366.9781	QS
(2019 GM1)	1.0035	0.0713	6.7415	367.1825	QS
419624 (2010 SO16)	1.0036	0.0754	14.5155	367.2296	HS
523728 (2014 ON344)	1.0037	0.3418	25.6937	367.2643	QS
(2014 HL199)	1.0038	0.2144	5.3991	367.3164	TP
(2021 TC1)	1.0041	0.2468	2.3095	367.4803	QS
138175 (2000 EE104)	1.0041	0.2931	5.2379	367.4857	TP
(2008 CQ116)	1.0041	0.1972	20.9921	367.4877	HS
(2015 XX169)	1.0043	0.1851	7.5983	367.59	TP
(2018 VB4)	1.0044	0.5979	13.5143	367.6745	QS
(2015 YQ1)	1.0045	0.404	2.4843	367.7049	QS
(2021 QH2)	1.0045	0.2864	10.3945	367.7193	QS
(2019 XS)	1.0045	0.3264	4.4472	367.7412	TP
(2020 TH6)	1.0047	0.2142	4.231	367.8407	QS

Table 11 Asteroids that can be reached from positive and negative perturbations from SL_1 and SL_2.

Asteroid Name	SL_1, +	SL_1, -	SL_2, +	SL_2, -
522684 (2016 JP)	Yes	Yes	No	No
(2019 AE3)	Yes	No	No	No
(2019 EO)	Yes	Yes	No	No
(2019 YB4)	Yes	Yes	No	No
(2007 FN3)	Yes	Yes	No	No
(2015 SO2)	Yes	Yes	No	No
(2020 GE1)	Yes	Yes	No	No
(2017 BG136)	Yes	Yes	No	No
(2018 PN22)	Yes	No	No	No
(2015 YA)	Yes	Yes	No	No
(2009 HE60)	Yes	Yes	No	No
(2009 WY104)	Yes	Yes	No	No
(2009 PC)	No	No	No	No
(2019 HS2)	Yes	Yes	No	No
(2021 BZ)	Yes	Yes	No	No
(2021 RE12)	No	No	No	No
(2021 OT)	Yes	Yes	No	No
(2016 CO246)	Yes	Yes	No	No
(2017 YQ5)	Yes	Yes	No	No
(2018 XW2)	Yes	Yes	No	No
(2017 SL16)	Yes	Yes	No	No
(2021 EY1)	Yes	Yes	No	No
(2021 XS4)	Yes	No	No	No
3753 Cruithne (1986 TO)	Yes	Yes	No	No
(2019 XQ1)	Yes	Yes	No	No
85770 (1998 UP1)	No	No	No	No
(2021 VH)	Yes	Yes	No	Yes
(2017 XQ60)	Yes	Yes	No	No
(2021 GN1)	Yes	Yes	No	No
(2014 OL339)	No	No	No	No
(2010 TK7)	Yes	Yes	No	No
(2021 KO2)	Yes	Yes	No	No
(2021 UN7)	No	No	No	No
(2016 CA138)	Yes	Yes	No	No
(2019 VL5)	Yes	Yes	No	No

(2020 PN1)	Yes	Yes	No	No
(2020 CX1)	Yes	Yes	No	No
(2020 XL5)	Yes	Yes	No	No
(2005 QQ87)	Yes	Yes	No	No
255071 (2005 UH6)	Yes	No	No	No
469219 Kamo‘oalewa (2016 HO3)	Yes	Yes	No	No
138852 (2000 WN10)	Yes	No	Yes	Yes
164207 (2004 GU9)	Yes	Yes	Yes	Yes
(2020 PP1)	Yes	Yes	No	No
277810 (2006 FV35)	No	No	No	No
(2013 LX28)	Yes	Yes	No	No
(2018 AN2)	Yes	Yes	No	No
441987 (2010 NY65)	No	No	No	No
(2019 SB6)	Yes	Yes	No	No
(2021 BA)	Yes	Yes	No	No
(2019 GM1)	Yes	Yes	Yes	Yes
419624 (2010 SO16)	No	No	No	No
523728 (2014 ON344)	No	No	No	No
(2014 HL199)	Yes	Yes	No	Yes
(2008 CQ116)	No	No	No	No
(2021 TC1)	No	No	No	No
138175 (2000 EE104)	Yes	Yes	No	No
(2015 XX169)	Yes	Yes	No	No
(2018 VB4)	No	No	No	No
(2015 YQ1)	Yes	Yes	No	No
(2019 XS)	Yes	Yes	No	No
(2021 QH2)	Yes	Yes	Yes	Yes
(2020 TH6)	Yes	Yes	No	No

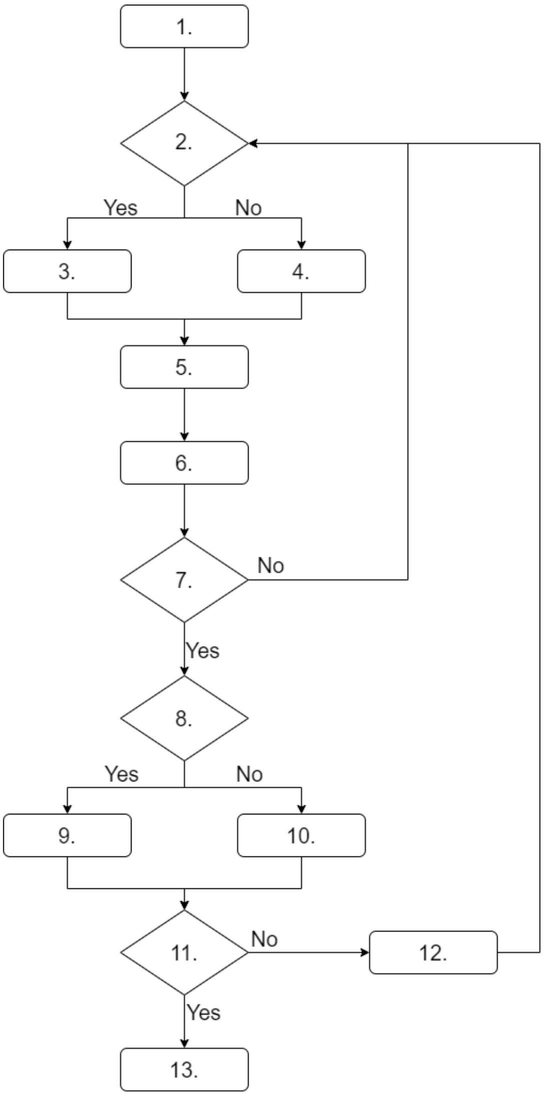

Fig. 13 Sequence selection flowchart

Step	Name	Description
1.	Start.	Start the sequence selection algorithm.
2.	First leg check.	Check if the current leg is the first leg of the trajectory.
3.	Initial leg variables.	If it is the first leg, randomly generate an initial date, cone, and clock angle.
4.	Sequential leg variables.	If it is not the first leg, randomly select a previous leg carried forward from step 12 to use as the starting point, as well as cone and clock angles.
5.	Propagation.	Propagate forward in time for two years.
6.	Fly-by analysis.	Analyse the motion of the spacecraft within the propagation time relative to the target asteroids.
7.	Check number of MC runs for the current leg.	Check if the number of times the current leg has been randomly generated has reached the total number of MC runs to perform. If not, repeat steps 2-6.
8.	Check for fly-bys	Check if any of the propagated legs contain a fly-by distance of less than 5×10^5 km.
9.	Rank optimal fly-bys.	If there are fly-bys of less than 5×10^5 km, rank each fly-by in ascending fly-by time, then rank all other fly-bys by fly-by distance.
10.	Rank non-optimal fly-bys.	If there are no fly-bys of less than 5×10^5 km, rank all trajectories according to minimum fly-by distance
11.	Check mission lifetime.	Check if the nominal mission lifetime of ten years has been reached.
12.	Carry forward previous legs.	If the nominal mission lifetime has not been reached, select a set proportion of the optimal trajectories to use as initial conditions in step 4. Then repeat steps 2-11.
13.	Finish.	If the nominal mission lifetime is reached, return the trajectory with the most rendezvous.

Table 12 Sequence selection steps

3

Conclusions and Recommendations

The journal article in the main body of this thesis work investigated the generation and optimisation of sequences of co-orbital asteroids to visit using only a solar sail as the propulsion method. This objective can be split into two distinct sections - the first is the generation of fixed-angle trajectories to multiple co-orbital NEAs, and the second is the optimisation of these trajectories. This chapter discusses the conclusions related to these objectives, as well as introducing some recommendations for future work. section 3.1 presents the conclusions reached in the thesis work by answering the research questions which were introduced in section 1.3. This is followed by recommendations regarding future research into this area, with possible development on the findings of this thesis in section 3.2.

3.1. Conclusions

The conclusions drawn on this thesis work are divided into answers for each of the research questions outlined in section 1.3, followed by a reflection on the findings and the thesis methodology.

1. *Can solar sailing be used as a propulsion method to visit multiple co-orbital asteroids in a given mission length, and if so, how many asteroids can be visited?*

   The planned NEA Scout mission shows that solar sailing can theoretically be used as an effective propulsion method to visit a NEA [27]. Further, conceptual mission designs have shown that solar sailing can be used to visit multiple NEAs in a single mission, reducing the cost and increasing the scientific return of the mission [31, 32]. A theoretical solar sailing mission has also been designed to the quasi-satellite, co-orbital asteroid, 2016 HO_3 [29]. This past research suggests that solar sailing is a suitable propulsion method to visit multiple co-orbital asteroids, however to date there have been no missions designed or proposed to investigate this possibility. Thus, the research carried out in this thesis aimed to further investigate the use of solar sailing for this purpose.

   The second element of this research question aims to investigate how efficient a solar sailing mission to multiple co-orbital NEAs can be. This efficiency refers to the number of encounters that can occur within a given mission lifetime. The developed sequence selection algorithm which generates trajectories to multiple co-orbital NEAs with fixed cone and clock angles for each transfer was capable of generating a trajectory with 18 encounters in just over 9 years, which is an encounter on average every six months. This value is found with limited tuning of the algorithm parameters, however it could conceivably be increased by running more simulations with a larger range of seed values and different parameter settings.

2. *Which of the co-linear artificial Lagrange points, SL_1 or SL_2, provides an initial position for more optimal trajectories?*

   Both of the co-linear Artificial Equilibrium Points (AEPs), SL_1 and SL_2, were investigated in this thesis to analyse their suitability as departure locations. These were selected initially to investigate as there are upcoming planned missions to both the L_1 and L_2 Lagrange points which could be used as a ride-share.

An initial search space analysis was performed on combinations of cone and clock angles when departing either the SL$_1$ and SL$_2$ point. This analysis determined that there is only a narrow 'window' of suitable combinations from SL$_2$ that do not intercept the Earth, whereas SL$_1$ has a wide range of possible combinations. This allows trajectories from SL$_1$ to encounter a wider range of targets, thus leading to trajectories with more encounters along the entire mission. Therefore, a ride-share on a mission to the L$_1$ point, such as NASA's Interstellar Mapping and Acceleration Probe (IMAP) mission to L$_1$ in 2025 [34], would provide a more suitable starting location for the mission. As proven in the journal article, the SL$_1$ point provides a much larger number of fly-bys than the SL$_2$ point and is therefore selected as the initial location for the full trajectory.

An initial search space analysis was performed on combinations of cone and clock angles when departing either the SL$_1$ and SL$_2$ point. This analysis determined that there is only a narrow 'window' of suitable combinations from SL$_2$ that do not intercept the Earth, whereas SL$_1$ has a wide range of possible combinations. This allows trajectories from SL$_1$ to encounter a wider range of targets, thus leading to trajectories with more encounters along the entire mission. Therefore, a ride-share on a mission to the L$_1$ point, such as NASA's Interstellar Mapping and Acceleration Probe (IMAP) mission to L$_1$ in 2025 [34], would provide a more suitable starting location for the mission.

3. *How do the relative fly-by distances and velocities compare for a fixed-angle control law and an optimised control law?*

   A full trajectory is generated with the developed sequence selection algorithm. This trajectory uses a fixed-angle control law for each transfer between asteroids, and considers a fly-by to have occurred when the spacecraft comes within 5×10^5 km of a target, with no bounds on the fly-by velocity. The first leg of the generated full trajectory is then optimised using pseudospectral collocation methods through PSOPT.

   In the results and conclusions sections of the journal article, it can be seen that implementing PSOPT significantly improves the fly-by of the first leg. The optimised control law reduces the relative fly-by distance from $307,702$ km to 158.73 km, which is a 99.95% reduction, while the relative velocity was reduced from 4.7923 km/s to 4.3282 km/s, which is a reduction of 9.68%. This is a significant improvement over the fixed-angle control law that is originally implemented and demonstrates the importance of an optimisation stage. It is clear that the fly-by conditions for the optimised control solution are significantly better than those for the fixed control law, and based on these results each leg should be individually optimised for the fly-by conditions to improve the overall mission.

These answers to the research questions display that it is feasible and suitable to use a solar sail as a method of propulsion to visit multiple co-orbital NEAs. A solar sailing mission departing the AEP SL$_1$ can have 18 asteroid fly-bys within a mission duration of ten years. This mission could be used to further analyse and classify the target asteroids, which could have research benefits for the investigation into the early solar system, as well as aid in the development of planetary defense system and space mining targets. The limitless propulsion available for a solar sailing mission makes it a very attractive method for long term missions that can analyse multiple targets with one spacecraft. The overall cost of investigating each of these targets would be significantly reduced in a mission with multiple fly-bys.

3.2. Recommendations

This section describes a range of recommendations for future work to build on the findings of this thesis. These recommendations could improve the fly-by conditions of each asteroid as well as increase further the number of asteroid fly-bys for a given mission time. These recommendations are split into three categories: the dynamical model, the sequence generation scheme, and the optimisation.

- *Dynamical Model*

  A higher-fidelity dynamical model could be implemented to more accurately investigate the motion of a solar sail spacecraft targeting asteroids in the vicinity of the Earth. The implemented Circular Restricted Three Body Problem (CR3BPS) assumes circular motion of the Earth-Moon system and the Sun around a common barycenter. In reality, however, the bodies orbit in slightly elliptical motion. The Elliptical Restricted Three-Body Problem (ER3BP) is a slightly more complex representation of the dynamics that accounts for this eccentricity in the orbits. Implementing this may increase the accuracy of the findings.

Further, the CR3BPS assumes that there are no fourth-body perturbations acting on the system. However, in reality, there will be slight gravitational attractions from the various other bodies in the solar system. The influence of each of these bodies could be investigated to determine if they will have a considerable effect on the motion of the spacecraft, and if so the perturbation can be modelled as a fourth-body acceleration.

Similarly, the implemented dynamical model assumes no gravitational attraction from any of the target asteroids. Depending on the mass of the asteroid, a close approach may perturb the solar sail trajectory and influence the motion of the spacecraft. A similar fourth-body acceleration model could be implemented for the vicinity of each asteroid to account for this influence, should it prove to be considerable.

The research carried out in the paper assumes a ride-share to either the L_1 or L_2 Lagrange points, and then assumes an initial starting location of either the SL_1 or the SL_2 sub-Lagrange AEP. There is a disconnect between these Lagrange and sub-Lagrange points, and a connecting trajectory between L_1 and SL_1 is required in order to carry out the proposed mission. Heiligers and McInnes [35] investigated solar sail trajectories between AEPs, and a similar trajectory from L_1 to SL_1 could be implemented to overcome the disconnect in this research.

Finally, the solar sail acceleration model implemented in this research assumes an ideal sail with purely specular reflection of the incident solar radiation. In reality, there will be elements such as absorption, diffuse reflection, thermal emission [29, 36], or wrinkling [37, 38]. Each of these components can reduce the acceleration generated by the sail from the incident solar radiation pressure (SRP), which will have an effect on the trajectory of the spacecraft. Thus, modelling these imperfections can lead to a more-accurate solution which accounts for realistic influences on the performance of the sail. However, modelling these imperfections can require more computational power, as the calculation of the acceleration of the spacecraft involves a more complex equation with a larger number of variables, e.g. see [29]. A trade-off can be performed to determine if it is worth including these effects.

- *Sequence Generation*

  The sequence generation algorithm developed in this thesis project generates random control angle values and analyses the motion of the spacecraft with these fixed settings. This algorithm analyses only the relative position between the spacecraft and the target asteroid, and neglects the relative velocity. As seen in the journal article section, this approach can lead to fly-bys with quite a large relative velocity, which is sub-optimal for a rendezvous mission. The sequence generation algorithm could be extended to include the relative velocity between the target and the spacecraft. This could be included with a weight in order to find trajectories that minimise both relative position and velocity.

  Further, due to the large range of possible control angle values, launch date, and target asteroids, the algorithm can generate a different solution each time it is run with a different seed value. The number of times the algorithm can be run is limited by computational power, but running on a more powerful processor would increase the speed at which a solution can be generated, and thus the algorithm can be run for a wider range of seed values producing different solutions. Similarly, increasing the number of random combinations to propagate and analyse at each leg of the trajectory could increase the number of optimal fly-bys that would be found. This is again limited by computational power. Increasing both the number of trajectories generated for each leg and the number of times the algorithm is run could lead to an increase from 18 in the number of possible fly-bys within the nominal ten year mission lifetime.

  Finally, limited tuning was performed on the parameters of the sequence generation algorithm that can be adjusted. Further testing and tuning of this algorithm could lead to a better combination of parameters that could generate sequences with a larger number of asteroid fly-bys.

- *Optimisation*

  The final section of the journal article focuses on the optimisation of the first asteroid fly-by. It is clear from this section that the relative fly-by distance and velocity between the spacecraft and target asteroid can be reduced using the PSOPT implementation. Thus, a clear next step would be to further optimise each individual fly-by for the entire generated trajectory. This would lead to a fully optimised control profile minimising the relative fly-by distance and velocity for each target asteroid.

  PSOPT can be set up to run a problem with a number of 'phases', where each phase is optimised individually and the optimisation process also ensures there are no disconnects between phases, i.e. the end state of one phase matches the initial state of the next. In the journal article research this process is performed manually, first optimising the fly-by and then using the results for the second leg. The problem could be extended to include both legs as phases and then the entire fly-by with both legs could be optimised as one solution. This is more complex to set up. In theory, with sufficient time and processing power, the entire 18 fly-by trajectory could be set up as 18 different phases in a single PSOPT problem, and the software could optimise the entire trajectory as one solution.

A

Verification and Validation

This chapter discusses the verification and validation performed on the developed models and numerical techniques used throughout this thesis. These models and techniques are those used to obtain the solar sailing trajectories to multiple near-Earth asteroids presented in this thesis work. The dynamical model representing the Circular Restricted Three Body Problem (CR3BP), the solar sail model, and the target asteroid model are developed and verified in section A.1. The numerical integration scheme selected for use in this thesis is developed in section A.2. Finally, section A.3 discusses the optimisation methods utilised in the final stage of this thesis.

A.1. Dynamical Model

The mission design in this thesis focuses on developing a solar sailing trajectory to multiple co-orbital near-Earth asteroids. The dynamical framework used in this thesis that governs the motion of a solar sailing spacecraft is the solar sail augmented Circular Restricted Three Body Problem (CR3BPS). A dynamical model representing this CR3BPS is developed in *MATLAB*$^{(\mathrm{R})}$, first without a solar sailing acceleration then including it.

A.1.1. Circular Restricted Three-Body Problem

The CR3BP describes the motion of an infinitesimally small body m under the gravitational influence of two primary bodies m_1 and m_2, which orbit their common center-of-mass in perfect circles [39]. The mass of the first primary body, the Sun, is taken as $m_1 = 1.9886 \times 10^{30}$ kg, while the mass of the Earth is taken as $m_E = 5.9736 \times 10^{24}$ kg, and the mass of the Moon is taken as $m_M = 7.348 \times 10^{22}$ kg [40]. The Earth-Moon system is assumed to be a single body within the CR3BP and CR3BPS implemented in this thesis, so the mass of the second primary body, m_2, is taken as $m_2 = m_E + m_M$.

The units of mass, distance, and time are normalized in the CR3BP and CR3BPS. The unit of mass is taken as the total mass of the system, i.e. $m_1 + m_2 = 1$. Introducing the mass ratio $\mu = \frac{m_2}{m_1+m_2}$, the masses of the Sun and Earth-Moon system become $m_1 = 1 - \mu$ and $m_2 = \mu$, respectively. This leads to a mass ratio value of $\mu = 3.04086372908265 \times 10^{-6}$.

A dynamical representation of the CR3BP is developed in *MATLAB*$^{(\mathrm{R})}$. To verify the correct implementation, the equilibrium (Lagrange) points of this system can be found. These points are locations where the third body, m, when placed at rest, will have a net acceleration of zero. This means the gravitational and centripetal accelerations acting on the third body, m, are balanced.

The acceleration of a body within the CR3BP is given by [29]

$$\ddot{\mathbf{r}} + 2\boldsymbol{\omega} \times \mathbf{r} = -\nabla U \tag{A.1}$$

where $\mathbf{r} = [x,\ y,\ z]^T$ is the position vector of m in the synodic reference frame $C(x, y, z)$, $\boldsymbol{\omega} = [0,\ 0,\ 1]^T$ is the angular rotation vector of the reference frame, and U is the effective potential. Assuming the infinitesimally small body, m, in the CR3BP has zero initial velocity or acceleration, the acceleration of this body can be reduced to $\ddot{\mathbf{r}} = -\nabla U = 0$. The *fzero.m* function in *MATLAB*$^{(\mathrm{R})}$ is used to find where the total acceleration (the sum of the gravitational acceleration and centripetal acceleration) of the bodies is zero for the three co-linear Lagrange points, while the two triangular Lagrange points can be found analytically. The calculated locations in dimensionless units of these Lagrange points are shown in Table A.1. To verify the correct implementation of the *fzero.m* function and the analytical solution for the triangular points, the acceleration of a body placed at each of these equilibrium points is calculated. These accelerations are also shown in Table A.1, and these can be seen to be either zero or negligible for all points. This verifies that these calculated points are equilibrium points.

Table A.1: Calculated Lagrange point locations and accelerations.

	x [-]	y [-]	z [-]	a_x [-]	a_y [-]	a_z [-]
L_1	1.010075688	0	0	3.538836E-16	0	0
L_2	0.989985500	0	0	3.295975E-16	0	0
L_3	-1.000001267	0	0	-3.543357E-16	0	0
L_4	0.499996959	0.866025404	0	-3.540661E-17	-3.482208E-17	0
L_5	0.499996959	-0.866025404	0	-3.540661E-17	3.482208E-17	0

The Lagrange points within the Sun-(Earth+Moon) CR3BP can be seen in Figure A.1.

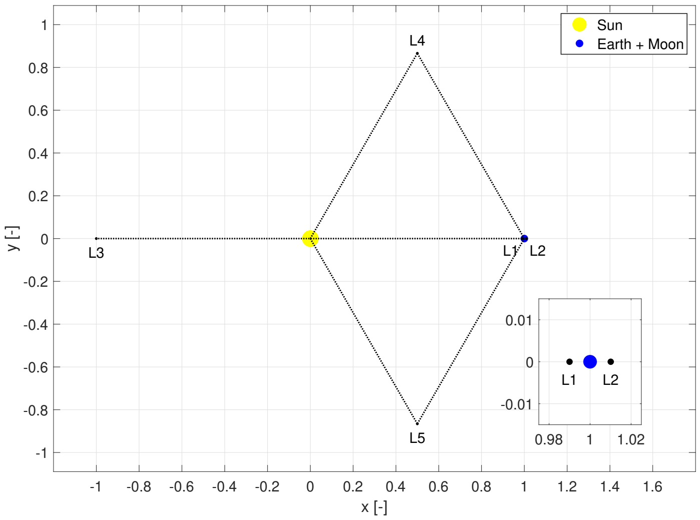

Figure A.1: Lagrange points in the Sun-(Earth+Moon) CR3BP.

The implementation of the model can be compared to literature to verify that it has been correctly developed. To verify this, a value from literature is used for the mass ratio and the Lagrange points of this system can be found. Prado [41] uses a mass ratio value of $\mu = 0.0000030359$ and finds the locations of Lagrange points within this system. This mass ratio value is introduced to the developed dynamical model and the Lagrange points are found in the same manner as above. These Lagrange points in the literature [41] as well as the calculated points are provided in Table A.2. It can be seen that these values match perfectly for the co-linear Lagrange points thus verifying the implementation, and for the triangular points the only difference is a slight rounding difference at the sixth decimal place. It can be assumed that this difference is negligible. Thus, the implementation of the dynamical model is shown to be correct.

A.1.2. Solar Sail Model

After development and verification of the CR3BP model, the solar sail augmented CR3BPS is developed. The introduction of a solar sail allows for the generation of further equilibrium points not limited to the Lagrange points in the classic CR3BP, known as AEPs. These AEPs depend on the lightness number of the sail, β, and the sail orientation.

To verify the implementation of the solar sailing model, AEPs can be generated and compared to values available in literature. The locations of the traditional Lagrange points L_1 and L_2 can be

Table A.2: Comparison of Provided and Calculated Lagrange point locations.

	Provided Values [41]		Calculated Values	
	x [-]	y [-]	x [-]	y [-]
L_1	1.0100702	0	1.0100702	0
L_2	0.9899909	0	0.9899909	0
L_3	-1.0000013	0	-1.0000013	0
L_4	0.4999969	0.8660254	0.4999970	0.8660254
L_5	0.4999969	-0.8660254	0.4999970	-0.8660254

shifted with the introduction of a solar sail. Farrés et al. [42] provides locations of co-linear AEPs, $SL_1$and SL_2, for varying sail lightness numbers. The mass ratio[1] used to calculate these values is $\mu = 3.04042340206596 \times 10^{-6}$. These provided values and those calculated using the developed *MATLAB*$^{\text{(R)}}$ code for the thesis are provided in Table A.3, where x_{SL_1} and x_{SL_2} are the values of the $x-$coordinate of the AEPs SL_1 and SL_2, respectively. It can be seen that the calculated values match those in the literature exactly, which verifies the implementation of the solar sail acceleration model.

Table A.3: Artificial Lagrange point $x-$locations provided in [42] and those calculated using the developed *MATLAB*$^{\text{(R)}}$ code.

	Provided in [42]		Calculated using *MATLAB*$^{\text{(R)}}$ code	
Lightness number β [-]	x_{SL_1} [-]	x_{SL_2} [-]	x_{SL_1} [-]	x_{SL_2} [-]
0.01	0.98873101897	1.00908250142	0.98873101897	1.00908250142
0.02	0.98716671573	1.00827979413	0.98716671573	1.00827979413
0.03	0.98525423949	1.00762463476	0.98525423949	1.00762463476
0.04	0.98299017728	1.00708319765	0.98299017728	1.00708319765
0.05	0.98040996743	1.00662972805	0.98040996743	1.00662972805

Further, the stability of these AEPs can be analysed by linearising the dynamical system, developing a Jacobian matrix, and calculating the eigenvalues ($\pm\tilde{\lambda}$, $\pm i\tilde{\omega}_i$) of this Jacobian. The eigenvalues associated with the Jacobian of the linearised system at the AEPs in Table A.3 are provided[2]. Similarly, these eigenvalues are calculated in the *MATLAB*$^{\text{(R)}}$ code. These provided eigenvalues and those calculated are given in Table A.4. It can be seen that the provided and calculated values match exactly, thus verifying the implementation of the linearisation of the dynamics of the system. The calculated eigenvalues have associated eigenvectors which are used to develop initial trajectories of the solar sail spacecraft. The method of calculating the eigenvectors has been verified, thus the associated eigenvectors are also verified.

Table A.4: Eigenvalues of AEPs

Provided Values								
β	x_{SL_1}	$\tilde{\lambda}$	$\tilde{\omega}_1$	$\tilde{\omega}_2$	x_{SL_2}	$\tilde{\lambda}$	$\tilde{\omega}_1$	$\tilde{\omega}_2$
0.01	0.98873	2.1408	1.8554	1.7779	1.0091	2.8875	2.3087	2.2421
0.02	0.98717	1.7847	1.6576	1.5745	1.0083	3.3052	2.5763	2.5152
0.03	0.98525	1.4763	1.4992	1.4122	1.0076	3.7303	2.854	2.7979
0.04	0.98299	1.2231	1.3818	1.2926	1.0071	4.1581	3.1376	3.086
0.05	0.98041	1.0259	1.3011	1.2107	1.0066	4.5854	3.424	3.3764
Calculated values from *MATLAB*$^{\text{(R)}}$ code								
β	x_{SL_1}	$\tilde{\lambda}$	$\tilde{\omega}_1$	$\tilde{\omega}_2$	x_{SL_2}	$\tilde{\lambda}$	$\tilde{\omega}_1$	$\tilde{\omega}_2$
0.01	0.98873101897	2.14076	1.8554	1.7779	1.00908250142	2.88751	2.3087	2.2421
0.02	0.98716671573	1.78466	1.6576	1.5745	1.00827979413	3.30517	2.5763	2.5152
0.03	0.98525423949	1.47628	1.4992	1.4122	1.00762463476	3.73030	2.8540	2.7979
0.04	0.98299017728	1.22313	1.3818	1.2926	1.00708319765	4.15807	3.1376	3.0860
0.05	0.98040996743	1.02589	1.3011	1.2107	1.00662972805	4.58536	3.4240	3.3764

---

[1] Provided by Jeannette Heiligers, co-author of [42]

[2] See footnote 1

While Lagrange points in the CR3BP are limited to three co-linear points and two triangular points, the introduction of a solar sail allows AEPs to exist outside of these locations. By varying the clock and cone angles of the solar sail, regions of AEPs with varying lightness numbers can be developed. Farrés and Jorba [43] developed regions of AEPs for varying lightness numbers around the Sun-Earth L_1 and L_2 points. These regions can be seen for lightness number values of $\beta = 0.01$ to $\beta = 0.05$ in Figure A.2a. Note, in A.2a, the Earth is placed at $[(\mu - 1), 0, 0]^T$ and the Sun is placed at $[\mu, 0, 0]^T$ in the system. Other than this convention, the dynamics and results will be the same as placing the Earth and Sun at $[(1 - \mu), 0, 0]^T$ and $[-\mu, 0, 0]^T$ respectively. The thesis code is adapted to adopt this convention, and Figure A.2a is reproduced as can be seen in Figure A.2b. It can be seen that the figure is reproduced exactly, thus verifying this element of the thesis dynamical model. Note that the axes in Figure A.2b have different scales, which are chosen to match the figure provided exactly.

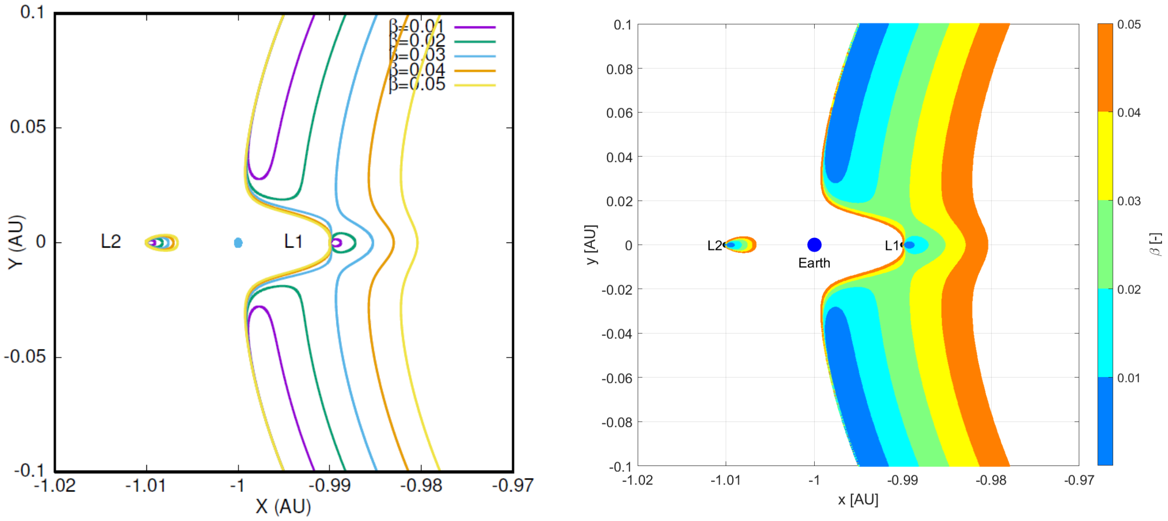

(a) Regions of AEPs for varying lightness numbers [43].

(b) Regions of AEPs produced by the thesis code.

Figure A.2: AEP contours

A.1.3. Asteroid Models

A database of the target asteroids is obtained from NASA's Jet Propulsion Laboratory (JPL) Horizons[3] system. The motion of each asteroid is obtained in a vector table for increments of one day over a 20 year period from 2023-2043. These vector tables include the position and velocity vectors of the asteroids in the J2000 inertial reference frame. The dynamical model in this project is given in the Sun-Earth synodic reference frame, so a reference frame transformation is required to model the motion of the asteroids in this synodic reference frame. The positions of the asteroids are rotated around an angle based on the right ascension of the ascending node Ω, the argument of periapsis ω, and the true anomaly θ of the Earth. For two-body motion the values of Ω and ω are fixed, and this assumption is valid in this thesis due to the assumption that the solar sailing spacecraft exerts no gravitational influence on the two larger masses. This more closely represents a circular orbit with no perturbations. After this rotation is performed, the x-coordinates of the asteroids are shifted by $-\mu$ to account for the origin of the synodic reference frame not being at the center of the Sun.

Heiligers et al. [29] provide the trajectory of asteroid 469219 Kamoʻoalewa (2016 HO_3) in a synodic Sun-Earth reference frame. The developed thesis code to transform the motion of the asteroids is tested on this asteroid over the same time period, 1960-2020. The motion of the asteroid as developed by Heiligers et al. [29] is provided in Figure A.3a. This motion is recreated with the developed thesis code and can be seen in Figure A.3b. It can be seen that these figures match, and thus the integration of the asteroid models into the synodic Sun-Earth reference frame has been verified.

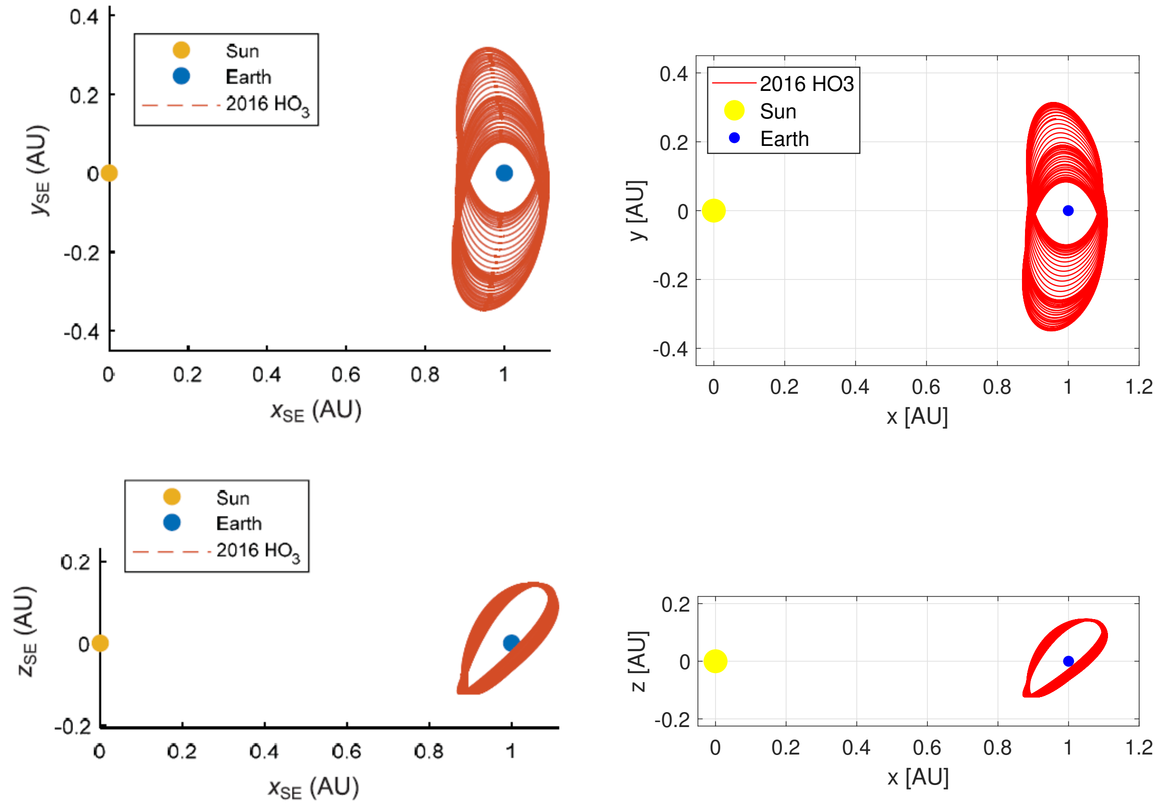

(a) Motion of Asteroid 2016 HO_3 [29].

(b) Motion of Asteroid 2016 HO_3 from the developed *MATLAB*$^{(R)}$ code.

Figure A.3: Asteroid 2016 HO_3.

---

[3] Jet Propulsion Laboratory. Small Body Database. Available at `https://ssd.jpl.nasa.gov/horizons/` [Access Date: 13 June 2022]

A.2. Integration Scheme

Through [33], it was determined that a Runge-Kutta 4(5) integrator would be suitable as it has both accuracy and speed of computation. This integrator is implemented directly in *MATLAB*$^{(R)}$ through the supplied *ode45.m* function. The implementation of this integrator in the thesis project and more specifically with the CR3BP is tested through propagation of CR3BP Halo orbits. Howell [44] performed extensive research on periodic orbits in the CR3BP and provides initial conditions for some Halo orbits. Initial conditions for a Halo orbit in a system with a mass ratio of $\mu = 0.04$ are provided as follows [44]

$$\mathbf{x}_0 = [\mathbf{r}_0 \;\; \dot{\mathbf{r}}_o]^T = [1.092791 \;\; 0 \;\; 0.309254 \;\; 0 \;\; -0.281140 \;\; 0]^T \tag{A.2}$$

where $\mathbf{x}_0 = [\mathbf{r}_0 \;\; \dot{\mathbf{r}}_0]^T$ is the initial state of the spacecraft at time t_0. Testing is performed on these initial conditions, by propagating the initial conditions forward in time for ten years with varying tolerance values, to determine a suitable tolerance. Ten years is chosen as this is the upper limit of the mission length considered in this thesis project.

The initial state provided, $\mathbf{x}_0$, lies on the $x - z$ plane. The state vector of the spacecraft within this Halo orbit is calculated when it crosses this plane after ten years and compared to the provided initial state. The difference with respect to the initial conditions is used to measure the accuracy of the integrator.

The results of this testing can be seen in Figure A.4, and it can be seen a tolerance of 10^{-9} provides a balance of numerical accuracy and computational time. Using a lower tolerance increases the run time required for the problem without increasing the accuracy of the results.

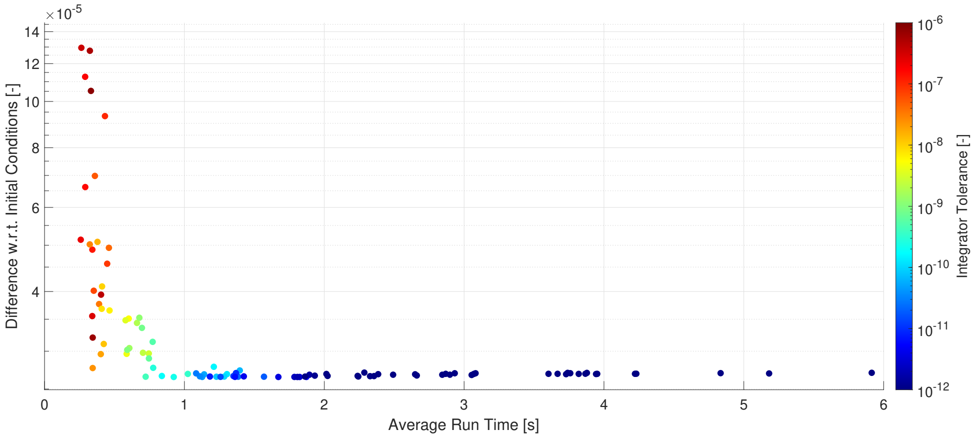

Figure A.4: Integrator Tolerance Testing

The developed dynamical model is then propagated forward for ten years using the provided initial conditions with a tolerance of 10^{-9}. It can be seen in Figure A.5 that there is little deviation from the Halo orbit with these provided initial conditions when propagated forward in time. The total deviation after ten years is 7.6959×10^{-4} from the initial condition. Therefore the integration scheme can be considered verified.

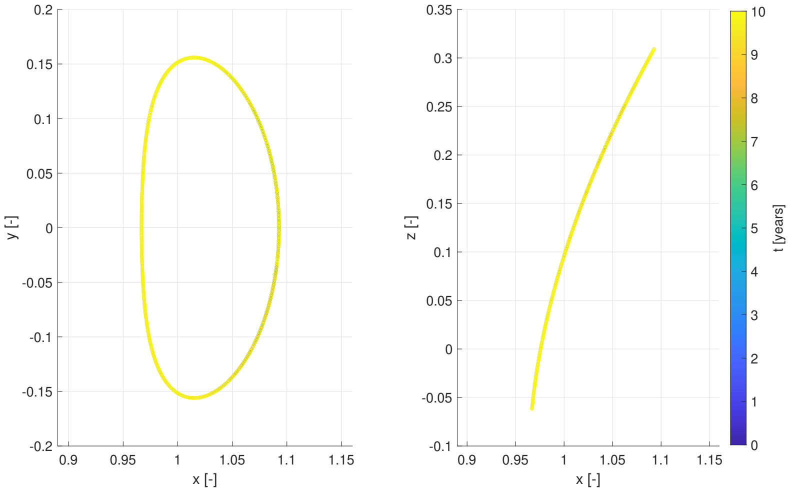

Figure A.5: Halo orbit with initial conditions provided by Howell [44].

A.3. Optimisation

The optimal control problem developed in the thesis is solved using PSOPT, an open-source direct pseudospectral method implemented in C++ [45]. PSOPT has been used for the optimisation of solar sailing missions in previous studies [29, 36, 42]. The implementation of the dynamical model in C++ is verified by comparing sample inputs to the developed *MATLAB*$^{(R)}$ implementation which produces the same output. The implementation of PSOPT is tested and verified by generating sample problems with known solutions and checking if PSOPT can reach these known solutions. PSOPT requires an initial guess as input to solve the optimal control problem. The PSOPT installation includes a number of sample optimisation problems. A small number of these sample problems are initially implemented to verify that PSOPT has been installed correctly.

Verification of a solar sailing problem implementation in PSOPT is performed by developing a relatively simple initial control problem. This is in the form of a minimum control effort problem, which is developed as follows. A known optimal trajectory with fixed cone and clock angles of $\alpha = 30°$ and $\delta = 0°$ is propagated forward in time for one year with the developed *MATLAB*$^{(R)}$ code. The initial state of the solar sail, $\mathbf{x}_0$, is selected randomly as

$$\mathbf{x}_0 = [0.95,\ 0.2,\ -0.1,\ 0,\ 0,\ 0]^T \tag{A.3}$$

A similar trajectory with fixed cone and clock angles of $\alpha = 35°$ and $\delta = 0°$ is also propagated forward in time for one year with the same initial state to be used as the initial guess. The bounds for the initial and final states set equal to those found in the known optimal trajectory, and the initial and final time bounds are set to exactly zero and one year respectively. PSOPT is set up to minimise the objective function, J, as follows

$$J = \int |\alpha_{out} - \alpha_{target}| \tag{A.4}$$

where α_{out} is the cone angle output at each node from PSOPT, and α_{target} is the known target cone angle. In this case $\alpha_{target} = 30°$. The integral symbol, $\int$ indicates that this is an integrand cost function, evaluated at each node.

This problem is implemented as described in PSOPT, using a consecutive mesh refinement of 50, 100, and 150 nodes, and a tolerance of 10^{-6}. Figure A.6 displays the trajectories of the initial guess, the known optimal solution, and the PSOPT solution. It can be seen that the initial and final states of the PSOPT solution match the initial and final states of the known optimal solution exactly. Further, the control angles for the initial guess and the PSOPT solution can be seen in Figure A.7. It can be seen that the output cone angle α_{out} matches the target cone angle of $\alpha = 30°$. For this problem, no constraints or bounds were placed on the clock angle. The PSOPT solution contains a time-variable clock angle, δ_{out}, which can be seen in Figure A.7.

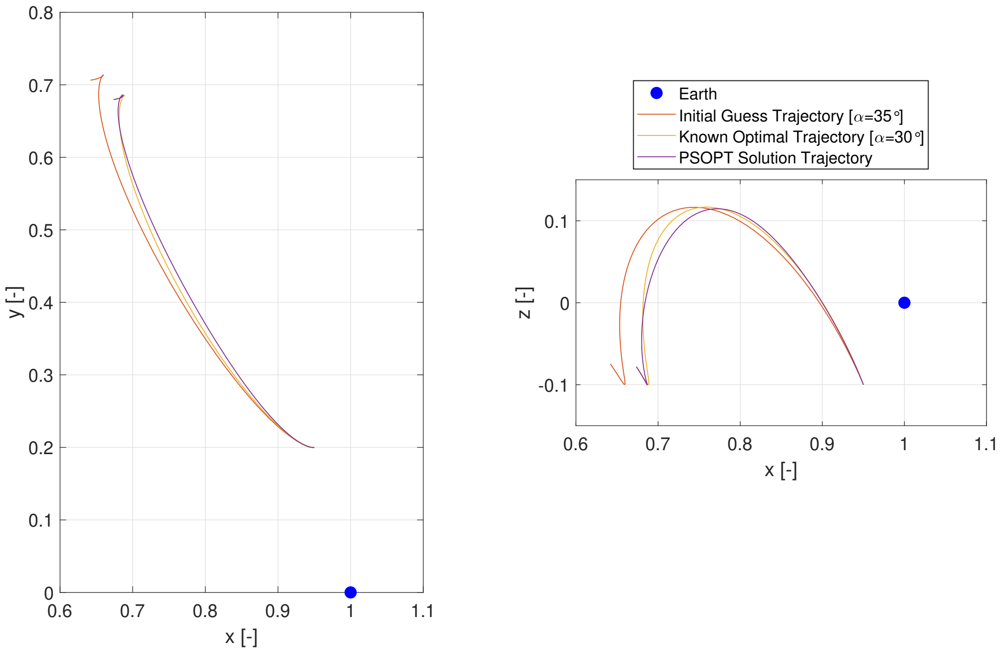

Figure A.6: PSOPT verification problem trajectories.

As all of the constraints placed on the problem are satisfied and the output cone angle, α_{out}, matches the target, the PSOPT solution found here is considered an optimal solution even though it does not match exactly with the known optimal input. As PSOPT converges to an optimal solution as desired, the implementation of a solar sailing optimal control problem is considered verified.

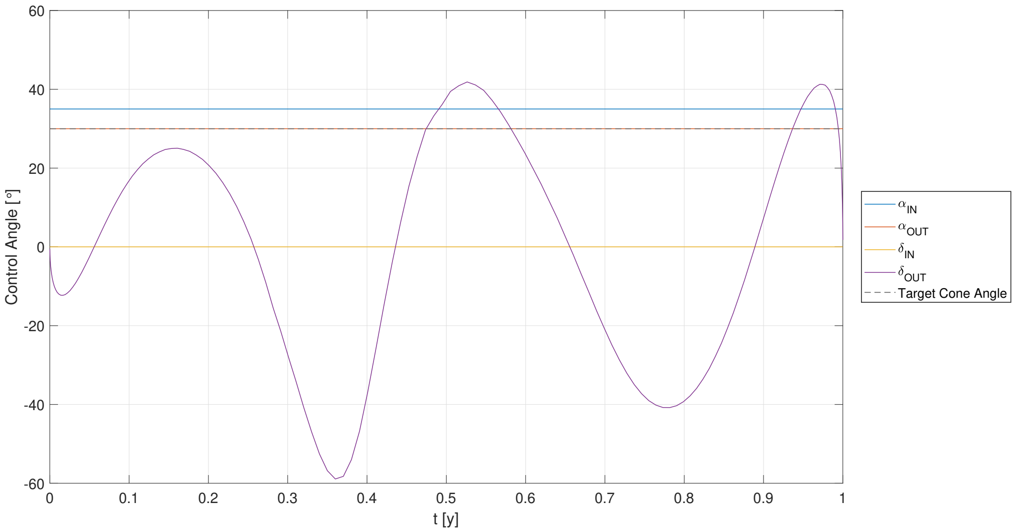

Figure A.7: PSOPT verification problem controls.

Bibliography

[1] JPL. NEO Basics, 2017, `https://cneos.jpl.nasa.gov/about/neo_groups.html` (Accessed: 2021-09-27).

[2] N. Atkinson. What is the Difference Between Asteroids and Comets? - Universe Today, 2014, `https://www.universetoday.com/33006/what-is-the-difference-between-asteroids-and-comets/` (Accessed: 2021-09-27).

[3] R. H. Nichols Jr. Chronological Constraints on Planetesimal Accretion. *Meteorites and the Early Solar System II*, 463:463–472, 2006.

[4] M. J. Drake, K. Righter, and E. Scott. Compositional Relationships Between Meteorites and Terrestrial Planets. *Meteorites and the Early Solar System II*, pages 803–828, 2003.

[5] M. S. Ahmedovich. Theory of Origin of Water in the Solar System. *European Journal of Engineering Research and Science*, 4(10):13–17, 2019. doi: 10.24018/ejers.2019.4.10.1486.

[6] C. M. Rumpf, H. G. Lewis, and P. M. Atkinson. Asteroid impact effects and their immediate hazards for human populations. *Geophysical Research Letters*, 44(8):3433–3440, 2017. ISSN 19448007. doi: 10.1002/2017GL073191.

[7] CNEOS. Impact Risk: Introduction, 2021, `https://cneos.jpl.nasa.gov/risk/intro.html` (Accessed: 2021-09-27).

[8] D. Sivolella. *Space Mining and Manufacturing: Off-World Resources and Revolutionary Engineering Techniques*. Springer, 2019. ISBN 9783030308803.

[9] C. de la Fuente Marcos and R. de la Fuente Marcos. A resonant family of dynamically cold small bodies in the near-earth asteroid belt. *Monthly Notices of the Royal Astronomical Society: Letters*, 434(1):1–5, 2013. ISSN 17453925. doi: 10.1093/mnrasl/slt062.

[10] C. de la Fuente Marcos and R. de la Fuente Marcos. Asteroid 2014 OL339: Yet another earth quasi-satellite. *Monthly Notices of the Royal Astronomical Society*, 445(3):2961–2970, 2014. ISSN 13652966. doi: 10.1093/mnras/stu1978.

[11] C. de la Fuente Marcos and R. de la Fuente Marcos. A trio of horseshoes: past, present and future dynamical evolution of Earth co-orbital asteroids 2015 XX169, 2015 YA and 2015 YQ1. *Astrophysics and Space Science*, 361(4):1–15, 2016. ISSN 1572946X. doi: 10.1007/s10509-016-2711-6.

[12] C. de La Fuente Marcos and R. de La Fuente Marcos. Using Mars co-orbitals to estimate the importance of rotation-induced YORP break-up events in Earth co-orbital space. *Monthly Notices of the Royal Astronomical Society*, 501(4):6007–6025, 2021. ISSN 13652966. doi: 10.1093/mnras/stab062.

[13] C. de la Fuente Marcos and R. de la Fuente Marcos. Asteroid 2017 FZ2 et al.: Signs of recent mass-shedding from YORP? *Monthly Notices of the Royal Astronomical Society*, 473(3):3434–3453, 2018. ISSN 13652966. doi: 10.1093/mnras/stx2540.

[14] R. Brasser, K. A. Innanen, M. Connors, C. Veillet, P. Wiegert, S. Mikkola, and P. W. Chodas. Transient co-orbital asteroids. *Icarus*, 171(1):102–109, 2004. ISSN 00191035. doi: 10.1016/j.icarus.2004.04.019.

[15] C. A. Giuppone, C. Beaugé, T. A. Michtchenko, and S. Ferraz-Mello. Dynamics of two planets in co-orbital motion. *Monthly Notices of the Royal Astronomical Society*, 407(1):390–398, 2010. ISSN 00358711. doi: 10.1111/j.1365-2966.2010.16904.x.

[16] V. V. Sidorenko, A. I. Neishtadt, A. V. Artemyev, and L. M. Zelenyi. Quasi-satellite orbits in the general context of dynamics in the 1:1 mean motion resonance: perturbative treatment. *Celestial Mechanics and Dynamical Astronomy*, 120(2):131–162, 2014. ISSN 15729478. doi: 10.1007/s10569-014-9565-4.

[17] C. D. Murray. The Earth's secret companion. *Nature*, 387(6634):651–652, 1997. ISSN 00280836. doi: 10.1038/42585.

[18] H. F. Levison, C. B. Olkin, K. S. Noll, S. Marchi, J. F. Bell, E. Bierhaus, R. Binzel, W. Bottke, D. Britt, M. Brown, M. Buie, P. Christensen, J. Emery, W. Grundy, V. E. Hamilton, C. Howett, S. Mottola, M. Pätzold, D. Reuter, J. Spencer, T. S. Statler, S. A. Stern, J. Sunshine, H. Weaver, and I. Wong. Lucy mission to the Trojan asteroids: Science goals, 2021. ISSN 26323338, `http://dx.doi.org/10.3847/PSJ/abf840`.

[19] C. R. McInnes. *Solar Sailing: Technology, Dynamics and Mission Applications*. Springer-Verlag Berlin Heidelberg, 1 edition, 2004. ISBN 978-3-540-21062-7.

[20] G. Vulpetti, L. Johnson, and G. L. Matloff. *Solar sails: A novel approach to interplanetary travel*. 2nd edition, 2015. ISBN 9781493909414. doi: 10.1007/978-1-4939-0941-4.

[21] E. F. Nichols and G. F. Hull. The Pressure Due to Radiation. *Proceedings of the American Academy of Arts and Sciences*, 38(20):559, 1903. ISSN 01999818. doi: 10.2307/20021808.

[22] O. Mori, Y. Shirasawa, Y. Mimasu, Y. Tsuda, H. Sawada, T. Saiki, T. Yamamoto, K. Yonekura, H. Hoshino, J. Kawaguchi, and R. Funase. Overview of IKAROS Mission. In M. Macdonald, editor, *Advances in Solar Sailing*, pages 25–43. Springer Berlin Heidelberg, Berlin, Heidelberg, 2014. ISBN 978-3-642-34907-2. doi: 10.1007/978-3-642-34907-2{_}3.

[23] Y. Tsuda, O. Mori, R. Funase, H. Sawada, T. Yamamoto, T. Saiki, T. Endo, K. Yonekura, H. Hoshino, and J. Kawaguchi. Achievement of IKAROS-Japanese deep space solar sail demonstration mission. In *Acta Astronautica*, volume 82, pages 183–188, 2013. doi: 10.1016/j.actaastro.2012.03.032.

[24] G. Vulpetti, L. Johnson, and G. L. Matloff. The NanoSAIL-D2 NASA Mission. In *Solar Sails : A Novel Approach to Interplanetary Travel*, Springer Praxis Books : Space Exploration TA - TT -, pages 173–178. New York, NY : Springer New York : Springer, 2015. ISBN 978-1-4939-0940-7. doi: 10.1007/978-1-4939-0941-4{_}16LK-https://tudelft.on.worldcat.org/oclc/5694009621.

[25] D. A. Spencer, B. Betts, J. M. Bellardo, A. Diaz, B. Plante, and J. R. Mansell. The LightSail 2 solar sailing technology demonstration. *Advances in Space Research*, 67(9):2878–2889, 2021. ISSN 18791948. doi: 10.1016/j.asr.2020.06.029.

[26] B. Betts, D. A. Spencer, J. M. Bellardo, B. Nye, A. Diaz, B. Plante, J. Mansell, M. A. Fernandez, C. T. Gillespie, and D. Garber. LightSail 2: Controlled solar sail propulsion using a CubeSat. In *Proceedings of the International Astronautical Congress, IAC*, volume 2019-Octob, 2019.

[27] L. McNutt, L. Johnson, D. Clardy, J. Castillo-Rogez, A. Frick, and L. Jones. Near-Earth Asteroid Scout. In *AIAA SPACE 2014 Conference and Exposition*, 2014. ISBN 9781624102578. doi: 10.2514/6.2014-4435.

[28] NASA. Advanced Composite Solar Sail System. *NASAfacts*, pages 6–7, 2020.

[29] J. Heiligers, J. M. Fernandez, O. R. Stohlman, and W. K. Wilkie. Trajectory design for a solar-sail mission to asteroid 2016 HO3. *Astrodynamics*, 3(3):231–246, 2019. ISSN 25220098. doi: 10.1007/s42064-019-0061-1.

[30] T. Hamasaki and J. Kawaguchi. Solar sail trajectory design for exploration of asteroids from/to space port around L2 point. In *Advances in the Astronautical Sciences*, volume 150, pages 3399–3417, 2014. ISBN 9780877036050.

[31] A. Peloni, M. Ceriotti, and B. Dachwald. Solar-sail trajectory design for a multiple near-earth-asteroid rendezvous mission. *Journal of Guidance, Control, and Dynamics*, 39(12):2712–2724, 2016. ISSN 15333884. doi: 10.2514/1.G000470.

[32] A. Peloni, B. Dachwald, and M. Ceriotti. Multiple near-earth asteroid rendezvous mission: Solar-sailing options. *Advances in Space Research*, 62(8):2084–2098, 2018. ISSN 18791948. doi: 10.1016/j.asr.2017.10.017.

[33] C. Buckley. Literature Study, Department of Aerospace Engineering, TU Delft, 2021.

[34] NASA, Princeton University, and Johns Hopkins Applied Physics Laboratory. IMAP Transfer Trajectory Initial State, 2019, `https://soma.larc.nasa.gov/stp/tdmo/pdf_files/2018-09-27_IMAP_Reference_LV_Transfer.pdf` (Accessed: 2022-05-23).

[35] J. Heiligers and C. R. McInnes. Agile solar sailing in three-body problem: Motion between artificial equilibrium points. *Proceedings of the International Astronautical Congress, IAC*, 7:5439–5451, 2013. ISSN 00741795.

[36] J. Heiligers, B. Diedrich, B. Derbes, and C. R. Mcinnes. Sunjammer: Preliminary end-to-end-mission design. *AIAA/AAS Astrodynamics Specialist Conference 2014*, 1(June 2016), 2014. doi: 10.2514/6.2014-4127.

[37] T. Pino, C. Circi, and G. Vulpetti. Wrinkling analysis for small solar-photon sails: An experimental and analytic approach for trajectory design. *Advances in Space Research*, 63(11):3675–3690, 2019. ISSN 18791948. doi: 10.1016/j.asr.2019.02.016.

[38] G. Vulpetti, D. Apponi, X. Zeng, and C. Circi. Wrinkling analysis of solar-photon sails. *Advances in Space Research*, 67(9):2669–2687, 2020. ISSN 18791948. doi: 10.1016/j.asr.2020.07.016.

[39] Z. E. Musielak and B. Quarles. The three-body problem. *Reports on Progress in Physics*, 77(6), 2014. ISSN 00344885. doi: 10.1088/0034-4885/77/6/065901.

[40] K. F. Wakker. *Fundamentals of Astrodynamics*. Institutional Repository, Delft University of Technology Library, 2015. ISBN 9789461864192. doi: 10.1007/978-3-319-09444-1{_}1.

[41] A. F. Prado. Orbital maneuvers between the lagrangian points and the primaries in the Earth-Sun system. *Journal of the Brazilian Society of Mechanical Sciences and Engineering*, 28(2):131–139, 2006. ISSN 16785878. doi: 10.1590/s1678-58782006000200001.

[42] A. Farrés, J. Heiligers, and N. Miguel. Road map to L4/L5 with a solar sail. *Aerospace Science and Technology*, 95:105458, 2019. ISSN 12709638. doi: 10.1016/j.ast.2019.105458.

[43] A. Farrés and A. Jorba. Solar sailing with invariant manifolds in the earth-sun system. *Proceedings of the International Astronautical Congress, IAC*, 7(October 2015):5323–5333, 2015. ISSN 00741795.

[44] K. Connor Howell. Three-dimensional, periodic, 'halo' orbits. *Celestial Mechanics*, 32(1):53–71, 1984. ISSN 00088714. doi: 10.1007/BF01358403.

[45] V. M. Becerra. Solving complex optimal control problems at no cost with PSOPT. In *Proceedings of the IEEE International Symposium on Computer-Aided Control System Design*, pages 1391–1396, 2010. ISBN 9781424453542. doi: 10.1109/CACSD.2010.5612676.